Active yaw control strategy for a hybrid offshore wind farm under typical wind conditions

Siyu Tao[1,2]*, Fuqing Jiang[1], Jisheng Yang[1], Hongxing Yang[2]*, Gang Zheng[3], Andrés E. Feijóo-Lorenzo[4], Ruiyang He[5]

1. College of Automation Engineering, Nanjing University of Aeronautics and Astronautics, Nanjing, 211106, China.
2. Department of Building Environment and Energy Engineering, Hong Kong Polytechnic University, Hong Kong, 999077, China.
3. Monash Biomedical Imaging, Monash University, Clayton, Victoria, 3800, Australia.
4. Department of Electrical Engineering, University of Vigo, Vigo, 36310, Spain.
5. School of Engineering, Cardiff University, Cardiff, CF243AA, U.K.

Corresponding Author: Siyu Tao (e-mail: taosiyu@nuaa.edu.cn)

Abstract: This paper proposes an active yaw control strategy for the hybrid offshore wind farms to enhance the offshore wind farm's total power generation. Firstly, a three dimensional yawed wake model is applied for calculating the power output of different types of wind turbines under active yaw control and the whole offshore wind farm. Next, the architecture of the proposed active yaw control system is demonstrated, and an optimization model is formulated. To solve this optimization problem, the quantum genetic algorithm is employed. Simulation results on a simplified layout of three wind turbines in a row and the Guishan offshore wind farm under three typical wind conditions demonstrate that the proposed strategy can effectively mitigate the inner-array wake effect in hybrid offshore wind farms. The results also suggest that applying active yaw control in the non-dominant wind directions and for small wind turbines in a hybrid offshore wind farm should be prioritized which yields the most significant improvements in

overall offshore wind farm power output. Additionally, the quantum genetic algorithm is shown to be an efficient and robust optimization tool for solving the optimal active yaw control problem in hybrid offshore wind farms.

Keywords: Mixed installation of wind turbines; hybrid offshore wind farm; active yaw control; 3D yawed wake model; quantum genetic algorithm; various wind conditions.

Nomenclature

Acronyms

AEP	Annual energy production	MPPT	Maximum power point tracking
AGC	Automatic generation control	NN	Neural network
AI	Artificial intelligence	OWF	Offshore wind farm
AYC	Active yaw control	PSO	Particle swarm optimization
CF	Capacity factor	2D	Two dimensional
DE	Differential evolution	3D	Three dimensional
DEL	Damage equivalent load	QGA	Quantum genetic algorithm
DL	Deep learning	RAM	Random access memory
GA	Genetic algorithm	RL	Reinforcement learning
GNN	Graph neural network	TLBO	Teaching learning-based optimization
ML	Machine learning	WT	Wind turbine
MPC	Model predictive control		

Variables

c_1	Personal learning coefficient in PSO	U_i	Wind velocity at the position of the i-th WT
c_2	Global learning coefficient in PSO	U_{ji}	Wind velocity at the position of the i-th WT considering only the wake of the j-th WT exists
C_{p0}^k	Power coefficient at zero yaw angle of the k-th type of WT	ΔU	Velocity deficit in the wake
C_t	WT thrust coefficient under AYC	$\Delta U_{ji}(x,y,z)$	Velocity deficit in 3D space at the i-th WT position considering only the wake of the j-th upstream WT exists
C_{t0}	WT thrust coefficient at zero yaw angle	u_0	Inflow wind speed

CF_{OWF}	Capacity factor of a hybrid OWF
d_0	WT rotor diameter
d_0^k	Rotor diameter of the k-th type of WT
d_{rt}	Distance between the WT rotor center and the tower center
h_0	WT hub height
h_0^k	Hub height of the k-th type of WT
M	Total number of WT types
$MaxIt$	Maximum iteration number
$nPop$	Population size of the optimization algorithm
N_k	Total number of the k-th type of WTs
p_c	Crossover rate in GA
p_m	Mutation rate in QGA and GA
P_{OWF}	Output power of a hybrid OWF
$P_{wt}^k(u_{h_0}^k,\gamma)$	The output power of the k-th type of WT under yaw condition
$P_{wt,r}^k$	Rated power of the k-th type of WT
r_0	WT rotor radius
S_y	Span-wise spacing between WTs
U_0	Inflow wind velocity
$u_{h_0}^k$	Wind speed measured at the hub height of the k-th type of WT
u_{in}	Cut-in wind speed of the WT
u_{out}	Cut-out wind speed of the WT
u_r	Rated wind speed of the WT
$u_{z_{ref}}$	Wind speed measured at the mast height
(x,y)	WT original coordinates
(x_θ,y_θ)	WT rotated coordinates under inflow wind direction θ
Y_{offset}	Span-wise location of the wake center
z_{ref}	Reference height
α	Wind shear index
γ	WT yaw angle
δ	Scale factor in the wake offset model
ζ	Expansion factor in the wake offset model
η	Cosine exponent related to the decay rate of the power coefficient
θ	Inflow wind direction
κ	Wake growth rate
ρ	Air density

1. Introduction

Offshore wind energy has emerged as a pivotal component of global sustainable energy portfolios, with increasing investments in large-scale offshore wind farms (OWFs) to meet decarbonization targets. To remain within the climate-critical 1.5°C global warming threshold, terawatt-scale wind capacity must be deployed globally by 2030. Annual offshore wind installations are projected to triple from 10.8 GW in 2023 to over 32 GW by 2028 [1].

Traditionally, OWFs have adopted homogeneous wind turbine (WT) configurations, installing identical WTs to simplify layout design, operation, and maintenance [2]-[7]. However, this approach may limit energy yield and economic efficiency, particularly in sites with varying water depths, wind conditions, and seabed properties. In response, recent research has increasingly explored hybrid OWFs that incorporate multiple types of WTs with different geometric and technical parameters [8]-[21]. Real-world implementations, such as the Borssele III/IV OWF in Netherlands, the Arkona OWF in Germany, and the Guishan OWF in China, have validated its feasibility of such heterogeneous configurations. Emerging wind farm optimization frameworks now systematically address heterogeneous WT configurations taking the selection and mixed-installation of WTs with diverse physical dimensions and various power curves into consideration [8]-[21]. These studies reveal that heterogeneous OWF configuration can yield multiple benefits, including increased total power output [8]-[10][15][20], lower energy costs [9][9][11]-[14][16]-[21], improved efficiency [8] or capacity factor (CF) [8][14][18], and more homogenized fatigue damages [8][17]. It has been noted in [10], when the vertical staggering between upstream and downstream WTs exceeds a critical threshold, strategically lowering downstream WT hub heights induces accelerated wake recovery which can yield enhanced power output that surpasses baseline configurations with identical WT hub height through optimized aerodynamic decoupling. Typically, the optimization applying larger WTs usually results in higher CF due to increased hub height and reduced wake effects through wider spacing. However, the feasibility of mixed-installations heavily depends on the WT mean capital costs difference [12].

The co-existence of multiple WT types with different geometric dimensions, *i.e.*, rotor diameters and hub heights in an OWF introduces unprecedented challenges in aerodynamic interaction, wake management, and load mitigation [8]. In an OWF, once WT positions are fixed, adjusting the wake distribution through WT control is an effective way to mitigate wake effects and fatigue load and to enhance power generation [22]. To alleviate the adverse effects induced by wake effect on the power reduction in OWFs, the active yaw control (AYC) strategy is proposed and widely applied [22]-[42]. This strategy intentionally misaligns upstream WTs via rotating their nacelles to steer wakes away from downstream ones, reducing energy losses. Using sensors and predictive models, optimal yaw angles are calculated in real time to achieve the goal of balancing between power gains from redirected wakes and slight individual WT power losses. By applying the AYC, the kinetic energy extraction ratio of the upstream and downstream WTs can be allocated and the overall efficiency of OWFs can be significantly improved [25]. For instance, Dou investigated the Horns Rev I OWF in Denmark and found that the AYC strategy exhibits superior optimization efficacy in directions experiencing acute wake deficit conditions [26]. In 2022, He developed a multivariate prediction framework employing machine learning-based fatigue loads and power prediction method for the AYC system and found that large yaw angles and high wind speeds can enhance prediction fidelity [27]. In 2023, Dong proposed a reinforcement learning (RL)-based AYC strategy which can enhance the long-term farm-level power production subject to strong wake effects without requiring analytical OWF models [31][31]. In 2024, Wang proposed a cooperative control strategy combined with start/stop control, AYC, and WT position optimization which outperforms using the aforementioned three control strategies separately [33]. A novel analytical model for yawed WTs, considering the effects of yaw angle, turbulence intensity and thrust coefficient was developed to predict the velocity deficit and the wake deflection in [34]. A data-driven model was put forward by Li to provide accurate predictions for the power generation of OWFs with arbitrary WT layouts, yaw angles and inflow wind conditions by encoding the OWF into a fully connected graph and processing through a graph transformer [35]. While this model [35] provides an efficient tool for optimal AYC of WTs, its validity remains unproven in hybrid OWFs with multiple WT types. More recently, Tu proposed a multi-fidelity framework based on the co-Kriging algorithm for predicting OWF power under yaw misalignment, finding that the positive yaw angles can significantly boost output and in a tandem configuration of WTs, the optimal distribution of yaw angles appears a decreasing trend from upstream to downstream [38]. The aforementioned studies demonstrate that integrating artificial intelligence (AI) techniques such as the machine learning (ML) techniques for improved wake modelling and prediction of WT response [27], deep learning (DL) for reduced-order modeling [23][36][42], RL for adaptive control strategies [31][31], neural network (NN) [32], graph neural network (GNN) [35] and surrogate model [36]-[39] for faster computation significantly enhances the efficiency and accuracy of AYC in OWFs and help WTs adapt to complex and dynamic wind conditions [40]. The objectives of the AYC optimization model majorly include the maximization of OWF total power generation [22][24]-[27][30]-[36][38] or OWF annual energy production (AEP) [7][37], the minimization of OWF power tracking error [23], the minimization of WT average fatigue load coefficient [24] or the WT damage equivalent load (DEL) [28][28] and to track the Automatic Generation Control (AGC) power signal [39]. However, current AYC methods are primarily designed for homogeneous OWFs and do not account for heterogeneous WT configurations [22]-[41]. This oversight can lead to sub-optimal yaw coordination and reduced overall OWF efficiency. Yaw angle optimization realized by AYC is vital in hybrid OWFs utilizing multiple types of WTs due to the compounded challenges of heterogeneous wake interactions and varying operational characteristics. Current methodologies exhibit significant limitations in resolving this problem due to the following critical factors. Firstly, existing techniques primarily employ two-dimensional (2D) yawed wake models [29] to calculate wake losses which can achieve sufficient accuracy for uniform OWFs. However, in hybrid OWFs, the coexistence of multiple WT types introduces significant variability in power curves, rotor diameters, and thrust coefficients. This heterogeneity results in asymmetric wake interactions, where larger upstream WTs can substantially diminish the energy yield of smaller downstream WTs. Although, conventional 2D wake models [29] can provide sufficient accuracy for uniform OWFs, they cannot adequately characterize vertical wake losses in hybrid OWFs, making them inapplicable for AYC optimization. Secondly, current investigations of AYC in OWFs typically examine system performance under simplified wind conditions, *i.e.*, either constant wind speed or unidirectional inflow conditions. The simplified wind condition analysis is only viable for uniform OWF with regular shapes and symmetrical layouts as it has minor effect on AYC optimization results. However, for hybrid OWFs mixed-installed with multiple types of WTs, it is highly possible that the OWFs have irregular shapes and asymmetrical layouts. Under this circumstance, wind comes from different directions with different speeds will have significant impacts on the AYC optimization results. Although there are are infinite combinations of wind speed and direction, at least the typical wind conditions analysis should be taken into account for the AYC optimization of the hybrid OWF.

Uncoordinated AYC causes sub-optimal wake steering, resulting in significant energy losses and accelerated fatigue damage, particularly for less robust WTs. To address these challenges, strategic yaw angle optimization dynamically direct wakes away from high-sensitivity WTs and balance total OWF output against component stress. Proper coordination unlocks 1-5% additional AEP for the OWF and extends WTs' lifespan-thereby enhancing project economics. Therefore, novel AYC strategies and algorithms are required for handling heterogeneous OWF while maintaining wake management benefits. Notably, there remains a significant absence in published articles addressing wake steering AYC strategies for hybrid OWFs with mixed-WT installations. The lack of theoretical models and validated control algorithms for the hybrid OWFs presents both a critical research challenge and an opportunity for innovation in OWF control optimization which are also the major contributions of this study. To fill this gap, this paper proposes a novel AYC strategy for the hybrid OWF for increasing power generation. The main contribution and novelty of this paper can be summarized as follows. Firstly, a three dimensional (3D) yawed wake model is used to estimate wake deficit considering WT size difference. Secondly, the QGA is used to solve the proposed hybrid OWF AYC optimization model. Thirdly, the effectiveness of the proposed AYC strategy for different types of WTs arranged in a straight line and in a real-world hybrid OWF is tested under typical inflow wind conditions.

The rest of this article is arranged as follows. The 3D yawed wake model and multiple wake synthesis method for the hybrid OWF AYC model are introduced and validated in Section 2. The optimization model and solution algorithm for the hybrid OWF under different wind conditions are proposed in Section 3. Case studies are carried out in Section 4, followed by Section 5, the conclusions.

2. Hybrid OWF AYC model

2.1. The 3D yawed wake model

In hybrid OWFs, WTs with various hub heights and rotor diameters are installed and therefore the vertical wind speed variations must be explicitly considered when estimating wake loss. To address this, the 3D yawed wake model proposed by Dou [26] is applied in this study, which can be described by (1). This model has taken wind shear into account and has been experimentally validated and therefore is suitable for the AYC modeling in the hybrid OWF. This model incorporates the effect of wind shear and has been experimentally validated, making it well-suitable for the AYC modeling in hybrid OWFs.

$$\frac{\Delta U}{U_0} = \left(1-\sqrt{1-\frac{C_t\cos\gamma}{8\sigma_{yaw}\sigma_z}}\right)\exp\left[-\frac{1}{2\sigma_{yaw}^2}\left(\frac{y-Y_{offset\_z}}{d_0\cos\gamma}\right)^2-\frac{1}{2\sigma_z^2}\left(\frac{z-h_0}{d_0}\right)^2\right] \tag{1}$$

where

$$\begin{cases}\sigma_{yaw} = \kappa x/(d_0\cos\gamma)+\sqrt{\beta}/5 \\ \sigma_z = \kappa x/d_0+\sqrt{\beta}/5 \\ \beta = \left(1+\sqrt{1-C_t\cos\gamma}\right)/\left(2\sqrt{1-C_t\cos\gamma}\right) \\ Y_{offset\_z} = \left(Y_{offset}-d_{rt}\sin\gamma\right)\exp\left[-\frac{1}{2\sigma_z^2}\left(\frac{z-h_0}{d_0}\right)^2\right]+d_{rt} \\ Y_{offset}/d_0 = \delta(C_{t0}\sin\gamma)^{\zeta}\cos^{2\zeta}\gamma\sqrt{x/d_0}+d_{rt}\sin\gamma/d_0 \\ \delta = \delta_0\cdot C_{t0}\end{cases}$$

where ΔU is the velocity deficit in the wake, U_0 is the incoming wind velocity, C_t is the WT thrust coefficient under AYC, $C_t = C_{t0}\cdot\cos^2\gamma$, C_{t0} is the WT thrust coefficient at zero yaw angle, γ is the WT yaw angle, κ is the wake growth rate, d_{rt} is the distance between the WT rotor center and the tower center, d_0 and h_0 are the WT rotor diameter and hub height, respectively, δ and ζ are the scale and expansion factors in the wake offset model, $\zeta = 0.75$, δ_0 is an empirical parameter, $\delta_0 = 0.607$, β is a parameter of the Gaussian wake model, Y_{offset} is the span-wise location of the wake center.

2.2. Validation of the 3D yawed wake model

The accuracy of the 3D yawed wake model has been validated in the horizontal and vertical planes by comparing with the wind tunnel measured data [26] as shown in Figs. 1 and 2. It can be seen that the 3D yawed wake model agrees well with the experimental measurements especially in the far wake region and it performs better under large yaw angles. As shown in Fig. 2, the wake shape in the wind tunnel experiments is not symmetrical about the hub height plane due to the interaction of the wake rotation with the tower shadow or ground.

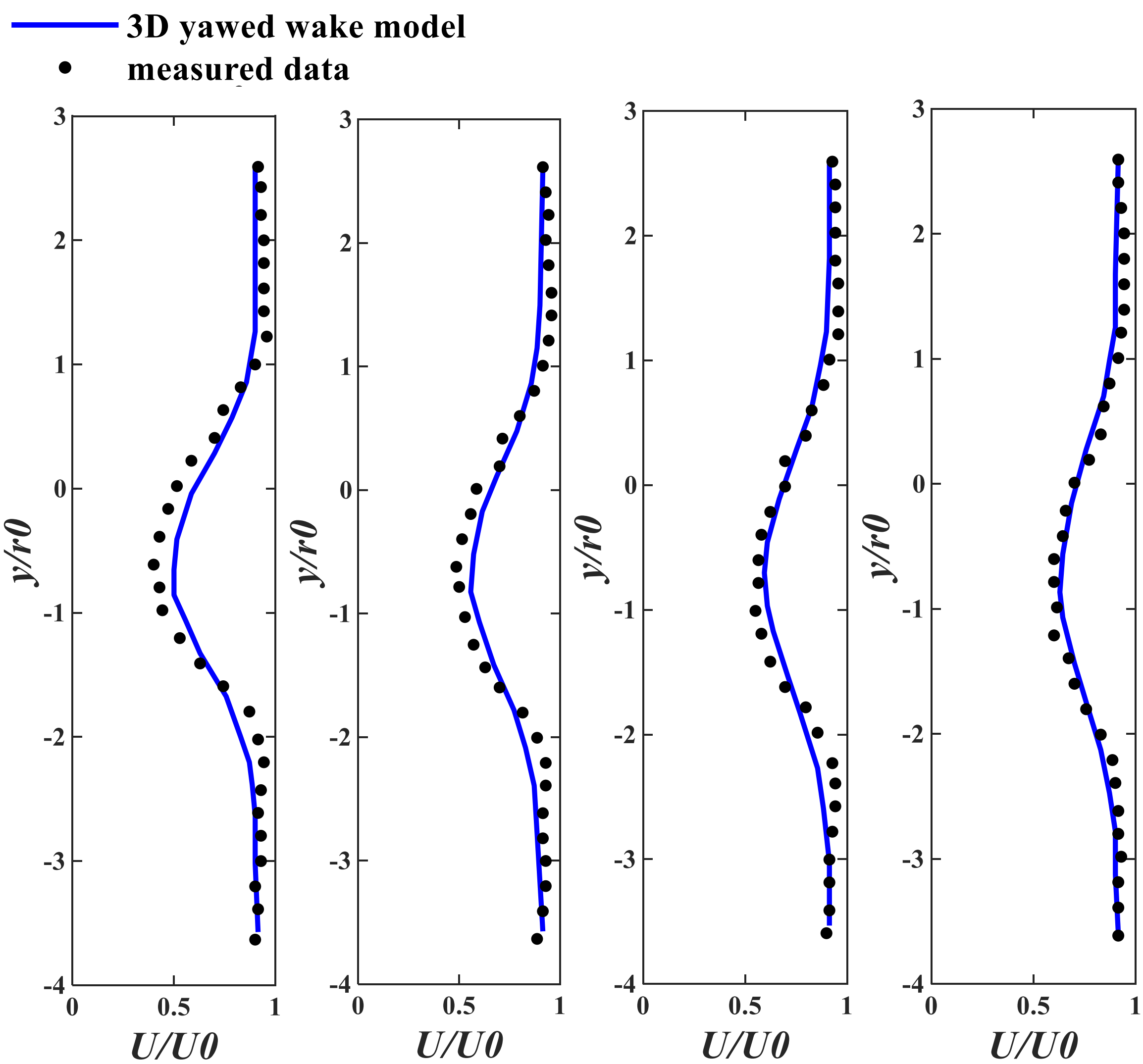

$5d_0$ $6d_0$ $7d_0$ $8d_0$

(a) $\gamma = 8°$

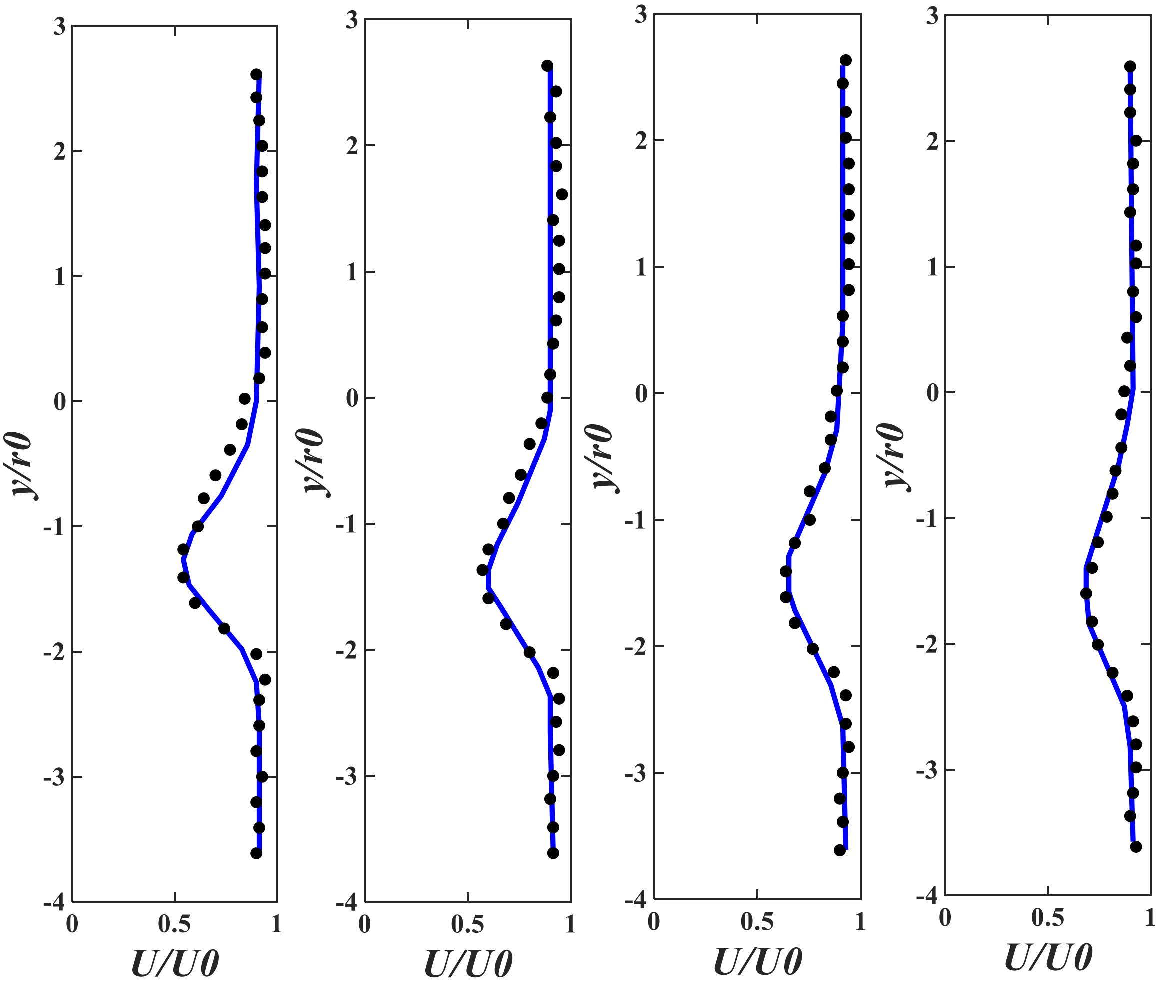

$5d_0$ $6d_0$ $7d_0$ $8d_0$

(b) $\gamma = 32°$

Fig. 1. Comparison of the 3D yawed wake model predicted value and wind tunnel measured data [26] in horizontal plane.

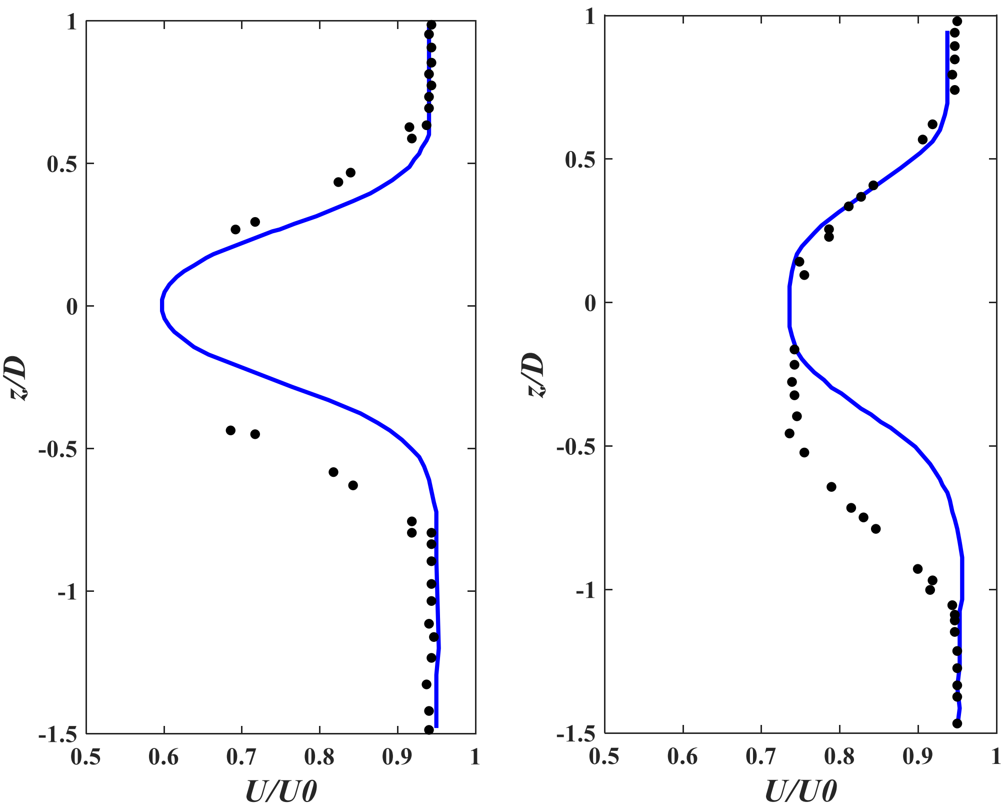

$5d_0$ $8d_0$

Fig. 2. Comparison of the 3D yawed wake model predicted value and wind tunnel measured data [26] in vertical plane.

2.3. Multiple wake synthesis method

For any inflow wind direction θ, the positional relationships between any upstream and downstream WT pairs are determined by rotating their original coordinates (x, y) to (x_θ, y_θ), by multiplying the transformation matrix in (2) [27].

$$\begin{bmatrix} x_\theta \\ y_\theta \end{bmatrix} = \begin{bmatrix} \cos\theta & \sin\theta \\ -\sin\theta & \cos\theta \end{bmatrix} \begin{bmatrix} x \\ y \end{bmatrix} \tag{2}$$

A downstream WT in the OWF is expected to be affected by the wakes of multiple upstream WTs. In this study, a linear superposition of the square of the velocity deficits is applied to synthesize the wakes generated by multiple upstream WTs, as given by (3) [26].

$$(U_0 - U_i)^2 = \sum_j (U_0 - U_{ji})^2 \tag{3}$$

where U_{ji} denotes the wind velocity at the position of the i-th WT considering that only the wake of the j-th WT exists, U_i represents the wind velocity at the position of the i-th WT.

The average stream-wise wake velocity at the position of the downstream WT behind yawed upstream WTs can be calculated by (4) [26].

$$u_{ji}(x) = u_0 - \int_{-a}^{a} \int_{-b+S_y}^{b+S_y} \Delta U_{ji}(x, y, z) dy\, dz \tag{4}$$

where $a = \sqrt{(d_0/2)^2 - [(y - S_y)/\cos\gamma]^2}$, $b = d_0 \cos\gamma$, $\Delta U_{ji}(x, y, z)$ is the velocity deficit in 3D space at the i-th WT position considering only the wake of the j-th upstream WT exists, S_y is the span-wise spacing between WTs.

2.4. WT and OWF output power calculation

Taking wind shear into consideration, before calculating the WT output power, the wind speed is firstly converted from the reference height z_{ref} to its hub height h_0^k by (5).

$$u_{h_0^k} = u_{z_{ref}} \left(\frac{h_0^k}{z_{ref}}\right)^{\alpha} \tag{5}$$

where $u_{z_{ref}}$ and $u_{h_0^k}$ are the wind speeds measured at the mast height and the hub height of the k-th type of WT, respectively, α is the wind shear index whose value is 0.1 in this study.

Suppose that there are M types of WTs installed in the hybrid OWF. The output power of the k-th type of WT under yaw condition, $P_{wt}^{k}\left(u_{h_0^k},\gamma\right)$ can be calculated by (6) [27].

$$P_{wt}^{k}\left(u_{h_0^k},\gamma\right)=\frac{1}{4}\rho\pi\left(d_0^k\right)^2 C_{p0}^{k} u_{h_0^k}^{3}(\cos\gamma)^{\eta} \tag{6}$$

where ρ is the air density, d_0^k is the rotor diameter of the k-th type of WT, C_{p0}^{k} is the power coefficient at zero yaw angle of the k-th type of WT and η is the cosine exponent related to the decay rate of the power coefficient which is 1.88 [27] in this study.

Suppose the total number of the k-th type of WTs is N_k, the output power of a hybrid OWF installed with M types of WTs under AYC, P_{OWF} can be obtained by summing up the output power of each WT, under their inflow wind speed $u_{h_0^k i}$ and yaw angle γ_i as expressed by (7).

$$P_{OWF}=\sum_{k=1}^{M}\sum_{i=1}^{N_k} P_{wt}^{k}\left(u_{h_0^k i},\gamma_i\right) \tag{7}$$

The CF of a wind farm is a measure of its actual energy output over a given period compared to its maximum possible output if it could be operated at full capacity continuously. The CF of a hybrid OWF, CF_{OWF} is defined by (8).

$$CF_{OWF}=\frac{P_{OWF}}{\sum_{k}^{M} N_k\cdot P_{wt,r}^{k}}\times 100\% \tag{8}$$

where the denominator is the rated capacity of the OWF, and $P_{wt,r}^{k}$ is the rated power of the k-th type of WT.

2.5. The hybrid OWF AYC system

The block diagram of the hybrid OWF AYC system is shown in Fig. 3. This control system operates as follows. Firstly, at each time interval of the control horizon, the inflow wind speed u_0 and wind direction θ are measured and fed into the farm-level controller. Based on these inputs, the controller computes the optimal yaw angle for each WT in the OWF. This optimization is carried out using the 3D yawed wake model and is solved by the quantum genetic algorithm (QGA) [43].

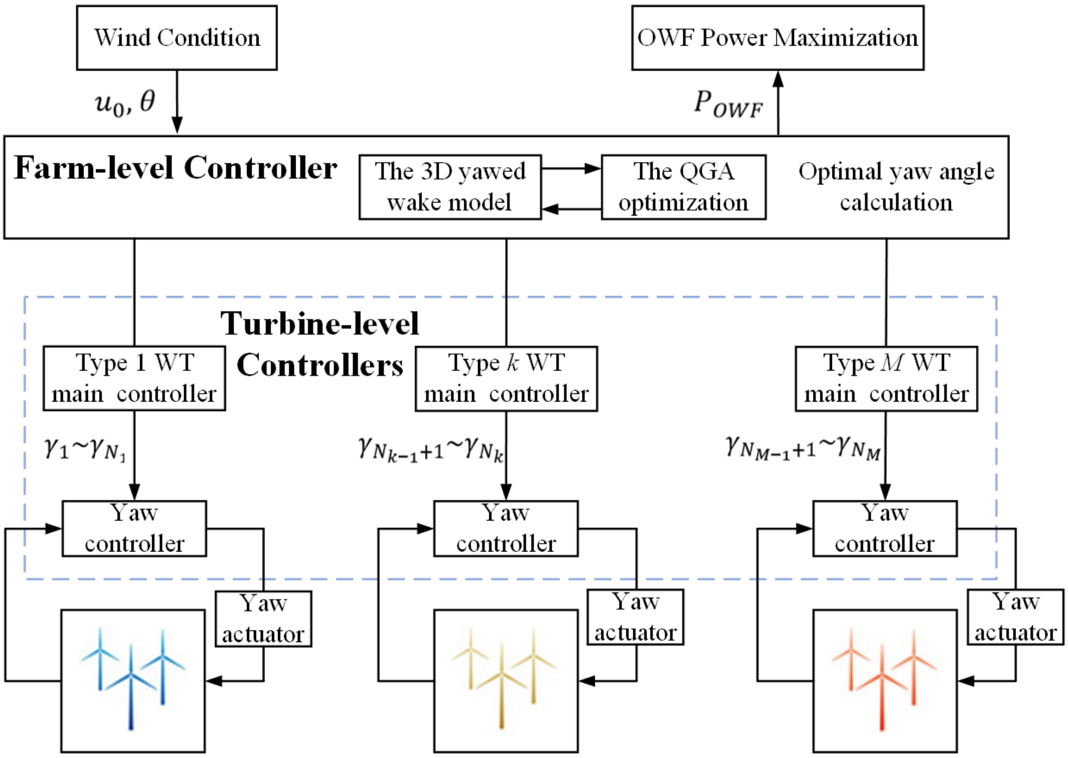

Fig. 3. Block diagram of the hybrid OWF AYC system.

The central controller determines the optimal yaw angle for each WT and transmits the corresponding command signals to the turbine-level controllers. These signals are then distributed to the main controllers of the different types of WTs. Each WT's yaw controller interprets the received command and directs the yaw actuator to adjust the nacelle orientation accordingly. The adjustment aligns the WT at a specified deflection angle relative to the incoming wind direction and maintains this position for optimal energy capture.

3. Optimization model and solution algorithm

3.1. Optimization model

Considering a hybrid OWF installed with M types of WTs, denoted as $WT_1, \cdots, WT_{N_1}, \cdots, WT_{N_k}, \cdots, WT_{N_{M-1}}, \cdots, WT_{N_M}$, the objective of its AYC is to maximize the total power generation by coordinating the yaw angle of each type of WT. Specifically, when yaw angles exceed 30°, the power loss of a yawed WT cannot be compensated by the power enhancement from downstream WTs [28]. Therefore, in this study, the yaw angle operating range is strictly limited to $\pm 30^{\circ}$ also to prevent structural overload on the WT nacelle, which can be expressed by (9).

$$\gamma^* = arg \max_{\gamma_i} \sum_k^M \sum_i^{N_k} P_{wt}^k \left(u_{h_0^k i}, \gamma_i \right) \tag{9}$$

$$s.t. \quad \gamma_i \in [-30°, +30°] \quad i = 1, 2, \cdots, \sum_{k=1}^M N_k$$

3.2. Solution algorithm

The QGA is a meta-heuristic optimization algorithm that integrates the principles of quantum computing with genetic algorithms (GAs). It is designed to enhance the performance of the GAs by leveraging the properties of quantum computation, particularly the superposition state characteristic of quantum bits (qubits). By utilizing qubits, the QGA enables a more efficient parallel search within the solution space. This parallelism significantly improves the algorithm's ability to avoid local optima and accelerates the convergence toward a global optimum. The key components of the QGA as follows: **1) Quantum Encoding:** The QGA employs qubits as fundamental units for information storage. By utilizing the superposition state of qubits, it represents the superposition of multiple states, thereby enabling more efficient parallel search within the solution space; 2) **Quantum Rotation Gate Operation:** The QGA applies the quantum rotation gate operation to enhance the breadth and depth of the search, optimizing the evolutionary process of chromosomes; 3) **Quantum Crossover and Mutation Operations:** The QGA utilizes quantum crossover and mutation operations to generate new quantum individuals. This increases the diversity of the search and helps prevent premature convergence to local optima.

The key steps of the QGA are summarized as follows.

Step1. *Initialization:* Create population of quantum chromosomes.

Step2. *Observation:* Generate classical solutions by measuring qubits.

Step3. *Evaluation:* Calculate fitness of each solution.

Step4. *Update:* Use quantum gates to evolve the population.

Step5. *Termination:* Check stopping criteria.

The pseudo code of the QGA in Algorithm 1 demonstrates its selection, crossover and mutation subroutines [43].

Algorithm 1 QGA

$H_P \leftarrow problem\_Hamiltonian$

$n \leftarrow number\_of\_registers$

$c \leftarrow number\_of\_qubits\_per\_register$

Initialization of the population

repeat

sort registers 1 to n according to H_P

reset registers $n/2$ to n

for $r = 1, 2, ..., n/2$

pseudo-clone register r to register $n/2 + r$.

end for

for $i = 1, 2, ..., n/4$

swap the last $c/2$ qubits of register $n/2 + 2i$-1

with the last $c/2$ qubits of register $n/2 + 2i$.

end for

mutate each qubit with probability p_m

until ending criteria is met $\vee G$ generations

The solution procedure of the hybrid OWF AYC optimization model by the QGA is shown in Fig. 4.

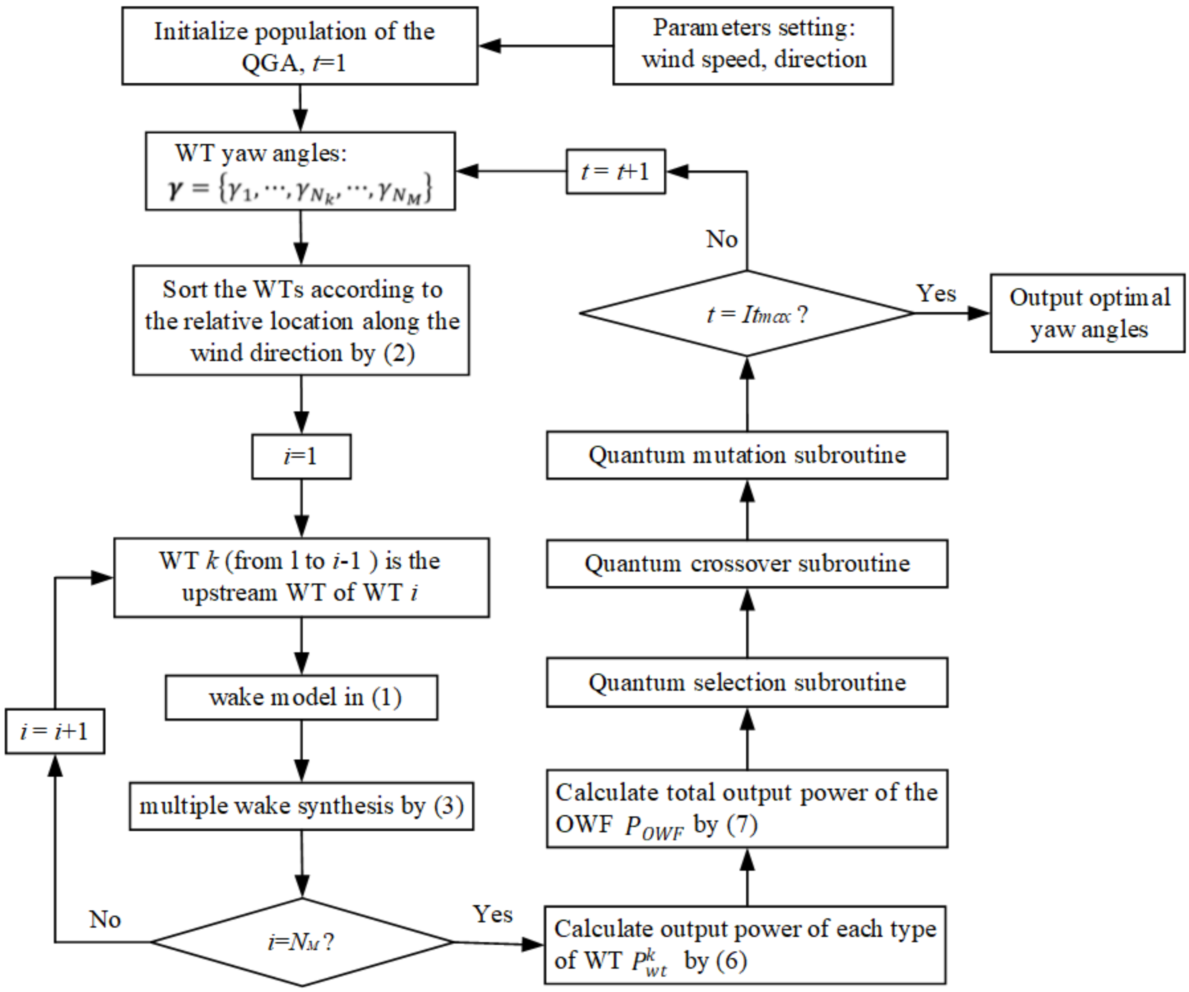

Fig. 4. Solution procedure of the hybrid OWF AYC optimization model by the QGA [43].

4. Case study

4.1. Test cases

The location and the layout of the Guishan OWF is shown in Fig. 5, which is located in Zhuhai, Guangdong Province of China (Latitude: 22°05'01"N~22°08'55"N, Longitude: 113°41'21"E~113°45'29"E), at a distance of about 20 km to the shore. There are thirty-four MySE3.0-112, seven MySE6.45-180, and eight D7000-186 WTs mixed-installed in this hybrid OWF and its total capacity is 203.15 MW. The WT types and positions in this case study are consistent with real-world engineering designs.

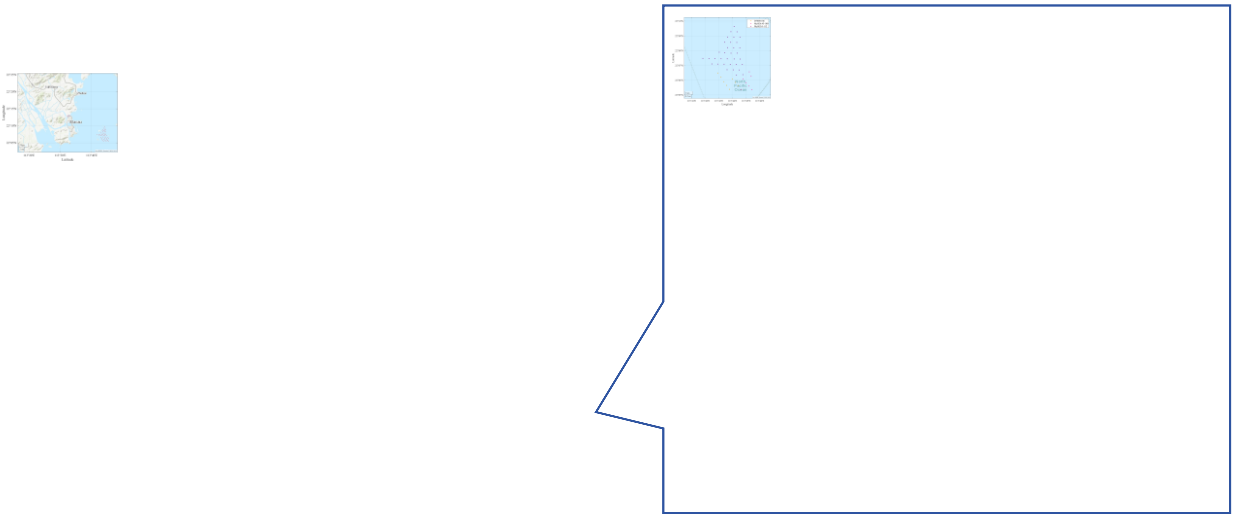

Fig. 5. Profile of the Zhuhai Guishan OWF [44].

Three types of WTs [45] are installed in the OWF, each with distinct thrust and power coefficients characteristics, as illustrated in Fig. 6. The geometric and technical parameters of these WTs are summarized in Table 1.

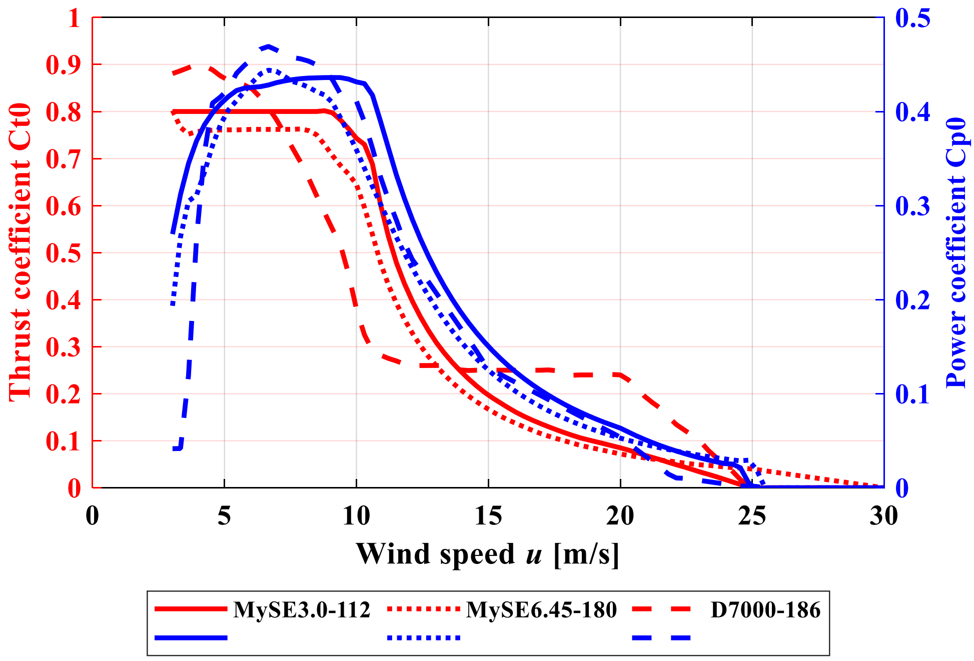

Fig. 6. Thrust and power coefficients curves of the three types of WTs [45].

Table 1

Geometric and technical parameters of the three types of WTs

WT type	Rated power $P_{wt,r}$ (MW)	Rotor diameter d_0 (m)	Hub height h_0 (m)	Cut-in wind speed u_{in} (m/s)	Rated wind speed u_r (m/s)	Cut-out wind speed u_{out} (m/s)
MySE3.0-112	3.00	112	90	3.0	11.0	25.0
MySE6.45-180	6.45	180	114	3.0	9.0	25.0
D7000-186	7.00	186	120	3.0	10.5	25.0

The parameters setting of the QGA are as follows. The population contains 4 individuals each with a chromosome length of 2 qubits and the population is therefore encoded as 8 qubits in total. The mutation probability of the chromosomes is set $p_m = \frac{1}{24}$, which means a mutation occurs in one of the 8 qubits, on average, every third generation.

4.2. Results and discussion

1) Optimal AYC of multi-types of WTs in a line

As demonstrated in Fig. 7, the test WTs are arranged in a straight line, ordered by their upwind sequence as WT1, WT2, and WT3. There are totally six possible combinations of WT sequences as listed in Table 2. The spacing of each WT pair is seven times of the front WT rotor diameter, *i.e.*, $D_{12} = 7d_{0,1}$ and $D_{23} = 7d_{0,2}$. The inflow wind speed u_0 measured at $z_{ref} = 100$ m is categorized into three levels: low wind speed at 6 m/s, medium wind speed at 8 m/s, and high wind speed at 10 m/s.

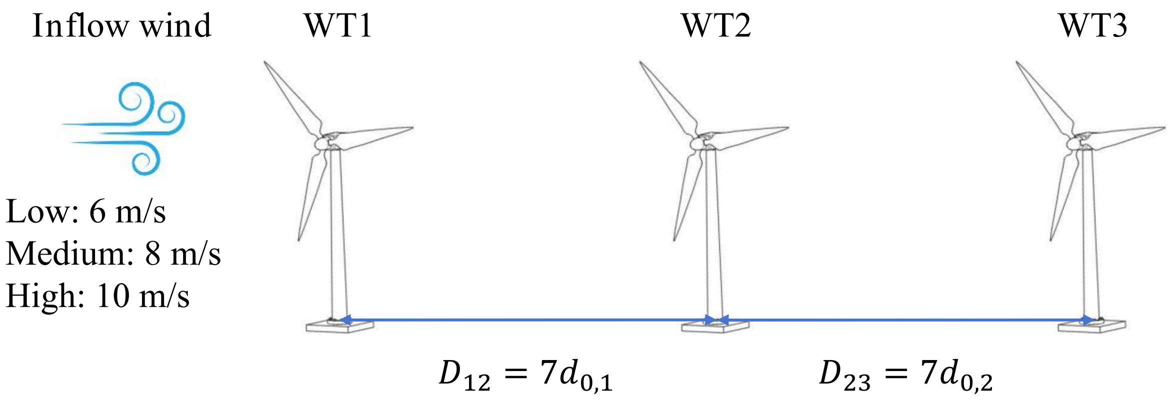

Fig. 7. WT ranking and spacing according to upwind sequence.

Table 2

WT upwind sequence combinations

Sequence No.	WT1	WT2	WT3
1	MySE3.0-112	MySE6.45-180	D7000-186
2	MySE3.0-112	D7000-186	MySE6.45-180
3	MySE6.45-180	MySE3.0-112	D7000-186
4	MySE6.45-180	D7000-186	MySE3.0-112
5	D7000-186	MySE3.0-112	MySE6.45-180
6	D7000-186	MySE6.45-180	MySE3.0-112

The output power of each WT before and after AYC in the six arrangements under the three typical inflow wind speeds are illustrated in Fig. 8. Their comparative wake contour maps are shown in Fig. 9 and the corresponding optimal WT yaw angles and power increment percentages brought about by AYC are given in Table 3.

It can be inferred from Fig. 8 that under the inflow wind speed $u_0 = 6\ \mathrm{m/s}$, the WTs arranged as Sequence No. 3 can produce the maximum total power ($P_{WT1} + P_{WT2} + P_{WT3} = 2{,}432.68$ kW) after AYC, while under the inflow wind speeds $u_0 = 8\ \mathrm{m/s}$ and $u_0 = 10\ \mathrm{m/s}$ the WTs arranged as Sequence No. 5 can produce the maximum total powers ($P_{WT1} + P_{WT2} + P_{WT3} =$

6,289.60 kW and $P_{WT1} + P_{WT2} + P_{WT3} = 16{,}782.367$ kW, respectively) after AYC. It should be noted that WT3 in Sequences 4 and 6 is basically in a newly-powered-on state. This phenomenon can be explained with the help of the wake contours in Fig. 9(a) and the optimal yaw angles in Table 3. Firstly, in Sequences 4 and 6, the WT in the last row is the smallest one, MySE3.0-112, which is prone to be totally merged in the wakes of the larger WTs, MySE6.45-180 and D7000-186 in the front rows. Although, under the AYC strategy, the total power generations of the WT sequences can be improved, this is based on the sacrifice of the power production of the smallest WT in the last row. As larger WTs have stronger abilities to capture more wind energy, the optimal yaw angles of the WTs in the medium row are not very large (+8.3° and -7.1°) in Sequences 4 and 6 to give their priority to produce more power. Secondly, the inflow wind speed in this case is relatively low ($u_0 = 6$m/s) which is much lower that the rated power of MySE3.0-112 WT ($u_r = 11.0$ m/s). Due to the unavoidable wake effects generated by the two large WTs in the front, the inflow wind speed of the WT in the last row will be decreased dramatically to be close to its cut-in wind speed ($u_{in} = 3.0$ m/s).

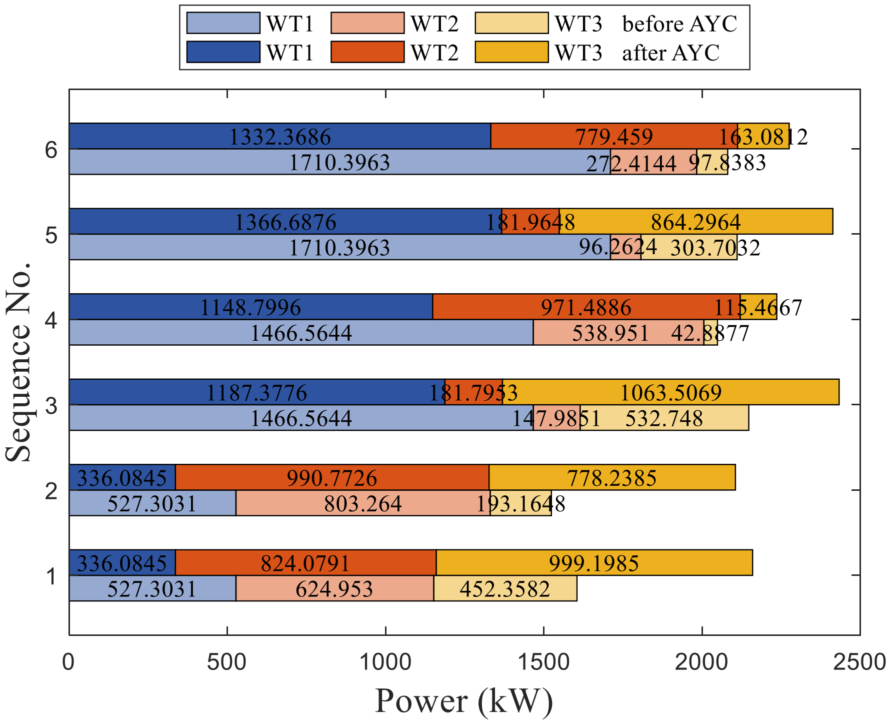

(a) $u_0 = 6$ m/s

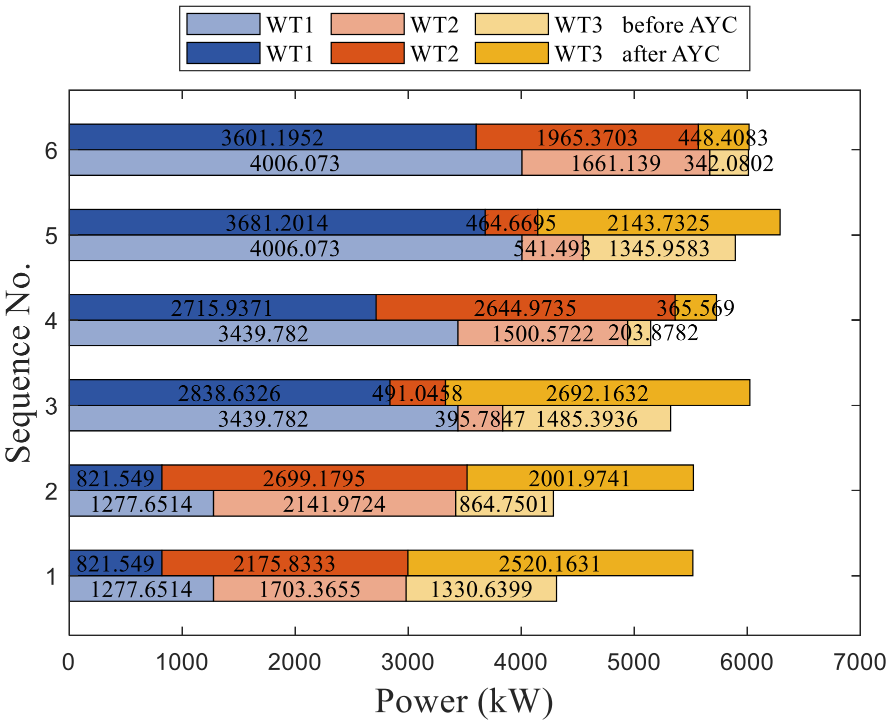

(b) $u_0 = 8$ m/s

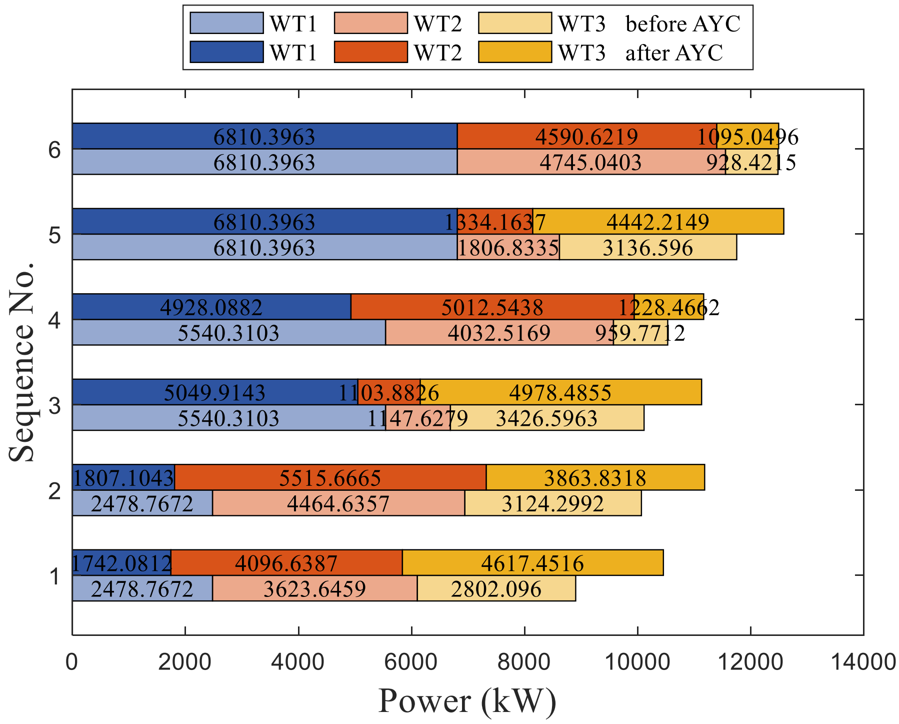

(c) $u_0 = 10$ m/s

Fig. 8. Output powers of the six WT sequences before and after AYC.

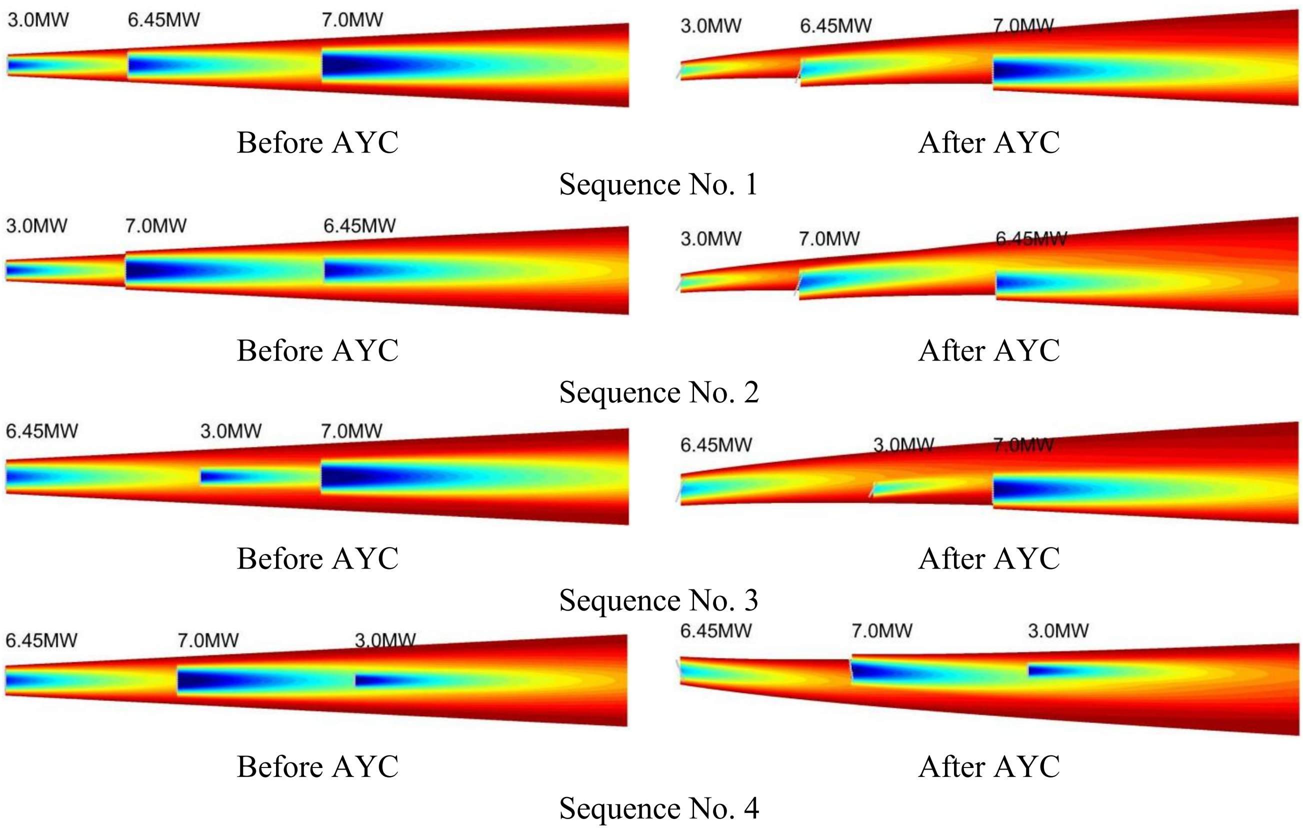

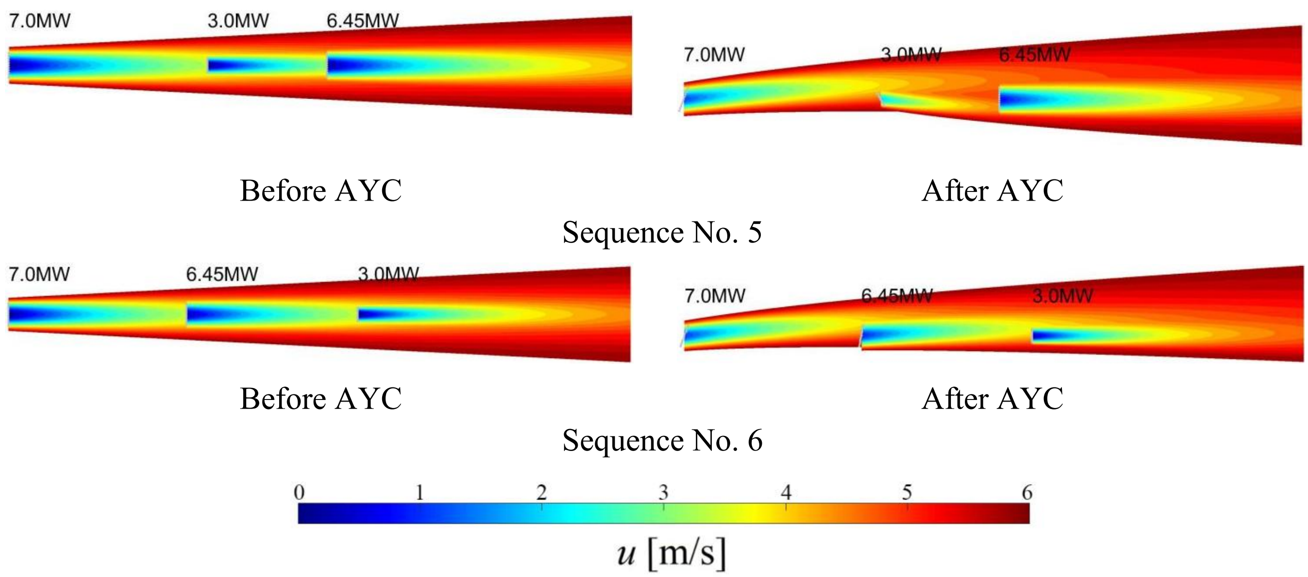
7.0MW
3.0MW
6.45MW
Before AYC
7.0MW
3.0MW
6.45MW
After AYC
Sequence No. 5
7.0MW
6.45MW
3.0MW
Before AYC
7.0MW
6.45MW
3.0MW
After AYC
Sequence No. 6
0
1
2
3
4
5
6
u [m/s]

(a) $u_0 = 6$ m/s

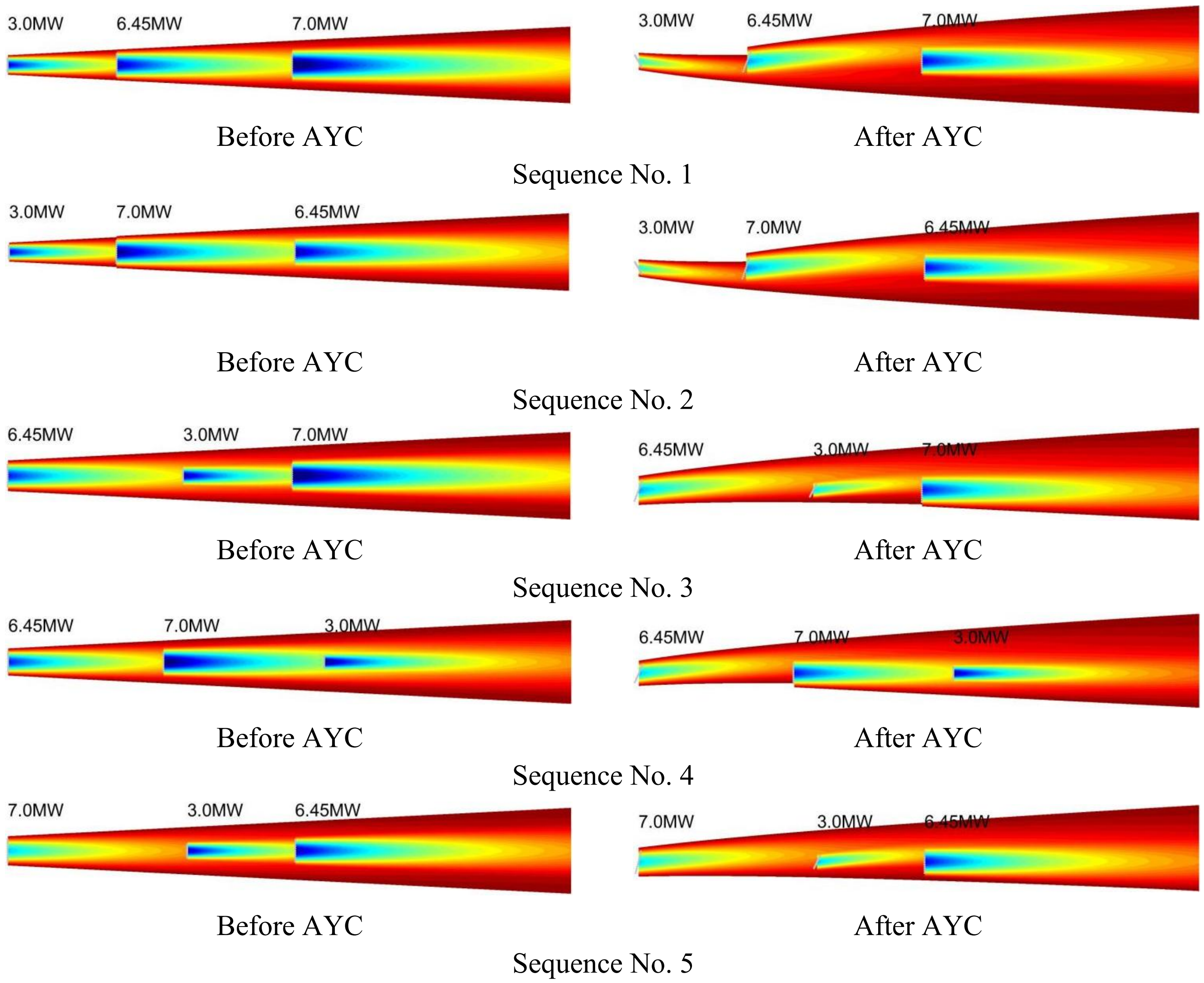
3.0MW
6.45MW
7.0MW
Before AYC
3.0MW
6.45MW
7.0MW
After AYC
Sequence No. 1
3.0MW
7.0MW
6.45MW
Before AYC
3.0MW
7.0MW
6.45MW
After AYC
Sequence No. 2
6.45MW
3.0MW
7.0MW
Before AYC
6.45MW
3.0MW
7.0MW
After AYC
Sequence No. 3
6.45MW
7.0MW
3.0MW
Before AYC
6.45MW
7.0MW
3.0MW
After AYC
Sequence No. 4
7.0MW
3.0MW
6.45MW
Before AYC
7.0MW
3.0MW
6.45MW
After AYC
Sequence No. 5

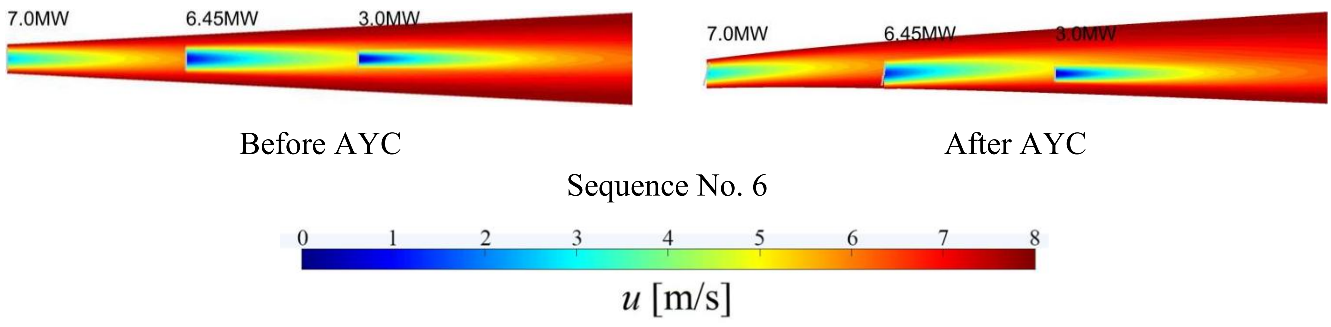

(b) $u_0 = 8\ \mathrm{m/s}$

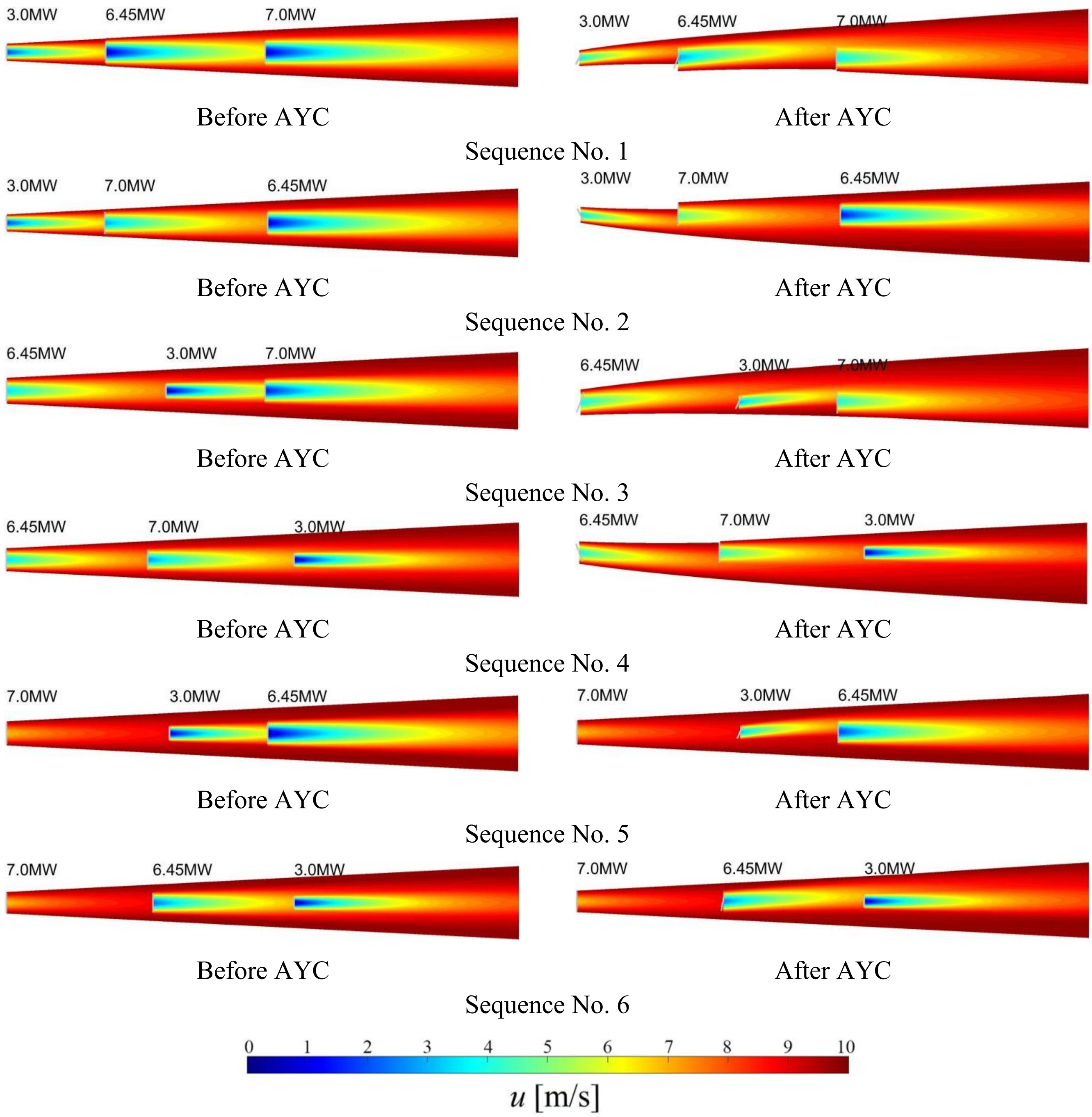

(c) $u_0 = 10\ \mathrm{m/s}$

Fig. 9. Comparative wake contour maps of the WT sequence at maximum power output under different inflow wind levels.

Table 3

Optimal yaw angles and power increment percentages of the WT sequences

Inflow wind speed		Optimal WT yaw angle			Power increment percentage
$u_0 = 6\ \mathrm{m/s}$		γ_1^*	γ_2^*	γ_3^*	
Sequence No.	1	-30°	-22.2°	0°	34.57%
	2	-30°	-22.1°	0°	**38.15%**
	3	-20.1°	-29.3°	0°	13.29%
	4	+21.5°	+8.3°	0°	**9.15%**
	5	-20.9°	+28.2°	0°	14.34%
	6	-22°	-7.1°	0°	9.34%
Inflow wind speed		Optimal WT yaw angle			Power increment percentage
$u_0 = 8\ \mathrm{m/s}$		γ_1^*	γ_2^*	γ_3^*	
Sequence No.	1	+30°	-21.5°	0°	27.97%
	2	+30°	-18.5°	0°	**28.90%**
	3	-20.9°	-28.4°	0°	13.17%
	4	-23.2°	0°	0°	11.32%
	5	-13.9°	-26.8°	0°	6.72%
	6	-15.6°	-9.1°	0°	**0.09%**
Inflow wind speed		Optimal WT yaw angle			Power increment percentage
$u_0 = 10\ \mathrm{m/s}$		γ_1^*	γ_2^*	γ_3^*	
Sequence No.	1	-27.6°	-19.8°	0°	**17.43%**
	2	+26.2°	0°	0°	11.11%
	3	-20.2°	-25.3°	0°	10.06%
	4	+22.2°	0°	0°	6.04%
	5	0°	-25.1°	0°	7.09%
	6	0°	-10.6°	0°	**0.10%**

Firstly, under the low inflow wind speed $u_0 = 6\ \mathrm{m/s}$, the total output powers of the WTs arranged as Sequences No. 2 and No. 4 increase the largest and lowest percentages (38.15% and 9.15%), respectively due to AYC. Under the medium inflow wind speed $u_0 = 8\ \mathrm{m/s}$, the total output powers of the WTs arranged as Sequences No. 2 and No. 6 increase the largest and lowest percentages (28.90% and 0.09%), respectively due to AYC. Under the high inflow wind speed $u_0 = 10\ \mathrm{m/s}$, the total output powers of the WTs arranged as Sequence No. 1 and No. 6 increase the largest and lowest percentage (17.43% and 0.10%) due to AYC, respectively. This demonstrates that AYC achieves maximum effectiveness for the smallest WT in the front row, while showing negligible impact for the largest WT in equivalent positions as for large-scale WTs, broader wake propagation limits the overall optimization benefits from yaw adjustments. Secondly, AYC demonstrates superior power enhancement efficacy at below-rated wind speeds ($u_0 \leq 8\ \mathrm{m/s}$), where wake effects are more persistent and energy recovery is critically needed. The lower the inflow wind speed is, the more pronounced the power gains from AYC. Thirdly, under the three inflow wind conditions, the optimal yaw angles of the WTs in the last row are all zero. Since the wake generated from the WT in the last row does not impact downstream WTs, there is no benefit in sacrificing its power output via yaw misalignment to enhance the overall WT string's efficiency. For an individual WT, the application of the maximum power point tracking (MPPT) strategy achieves optimal performance at zero yaw angle, *i.e.*, perfect alignment with the wind direction, maximizing energy capture efficiency. Lastly, under the high inflow wind speed $u_0 = 10\ \mathrm{m/s}$, some of the optimal yaw angles of the front and the intermediate WTs are zero. This can be explained as follows. On one hand, under high wind speed conditions, wake recovery accelerates. Wake recovery velocity increases by 20-30% at above-rated wind speeds, significantly shortening the downstream stabilization distance. On the other hand, according to Fig. 4, under high inflow wind speeds, the WT thrust coefficient asymptotically approaches a stable plateau, resulting in significantly reduced sensitivity of wake steering effectiveness to yaw angle variations.

2) Optimal AYC of the Hybrid OWF

The wind rose of the Guishan OWF is shown in Fig. 10 where the met mast height is $z_{ref} = 100$ m. According to Fig. 10, the three typical wind directions ($\theta =$ W, ESE, NNE) which represent the rare, medium and dominant wind directions and their corresponding wind speeds ($u_0 = 6, 8, 10$ m/s) which represent the low, medium and high wind speeds of this OWF are chosen as the three typical inflow wind conditions in this study and are demonstrated in Fig. 11.

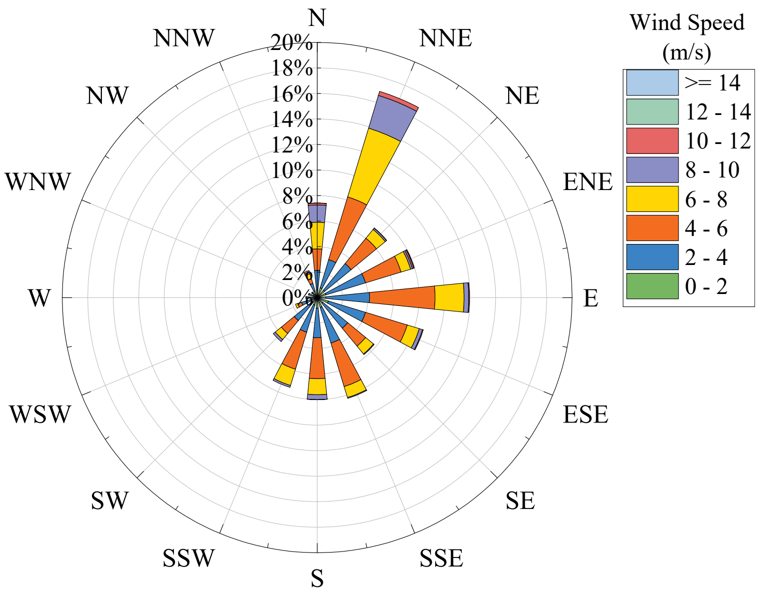

Fig. 10. Wind rose (1/Jan/2024-31/Dec/2024) [46].

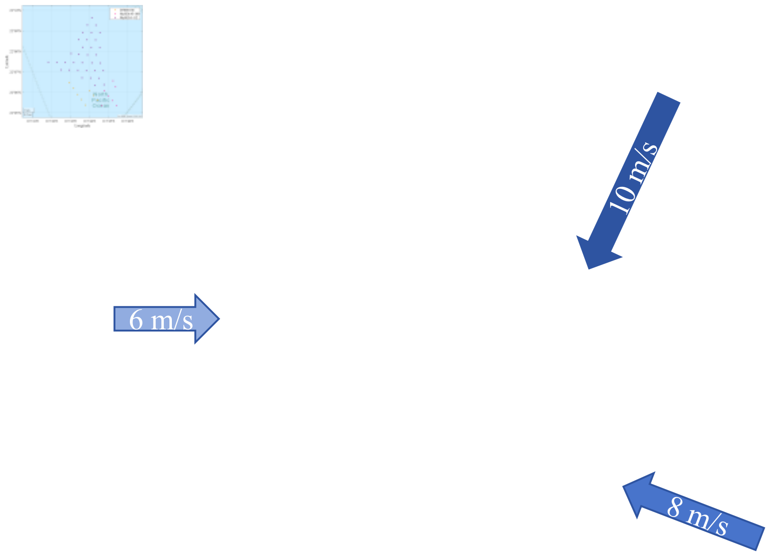

Fig. 11. Three typical wind conditions of the Guishan OWF.

The wake contours of the Guishan OWF without AYC under the three typical wind speeds and directions are shown in Fig. 12. In this scenario, each WT utilizes passive yaw control strategy, ensuring self-alignment with the wind direction. As a result, the yaw angle remains zero for each WT under all inflow wind conditions.

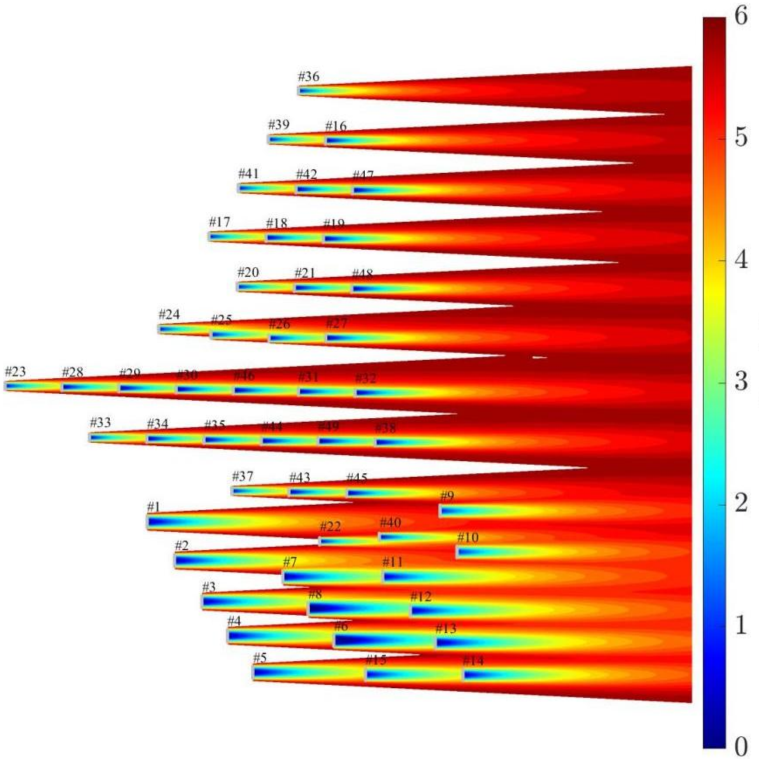

(a) Case 1: $\theta = \mathrm{W}, u_0 = 6$ m/s

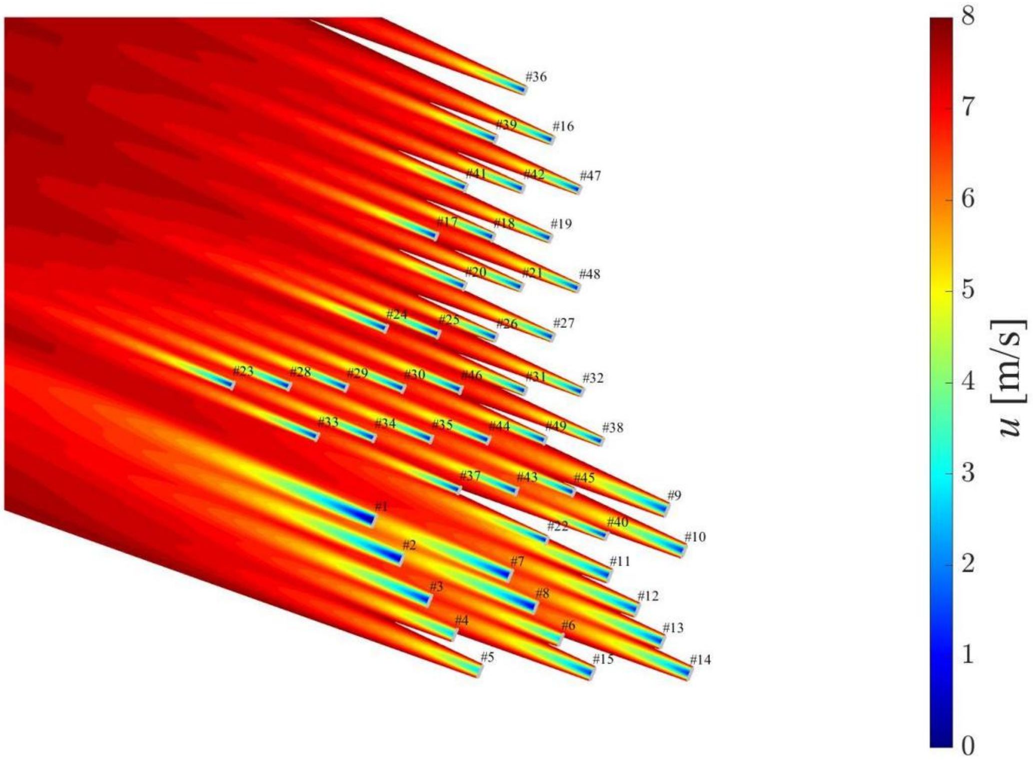

(b) Case 2: $\theta = \mathrm{ESE}, u_0 = 8$ m/s

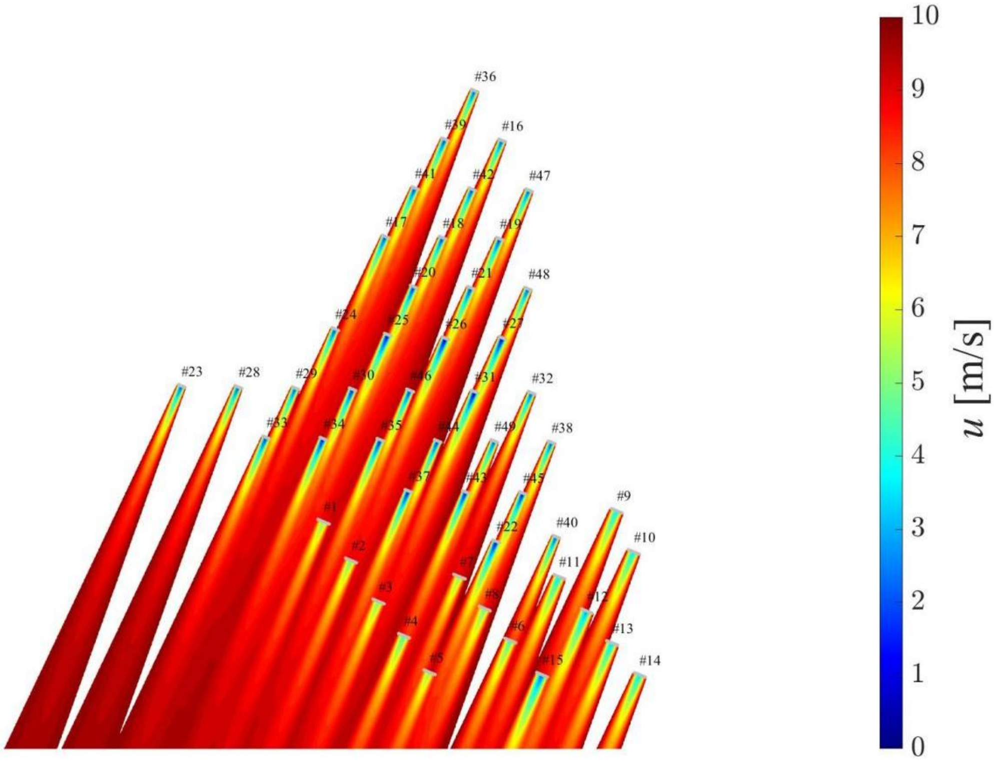

(c) Case 3: $\theta = \text{NNE}, u_0 = 10\ \text{m/s}$

Fig. 12. Wake contours of the Guishan OWF without AYC under typical wind speeds and wind directions.

The optimal WT yaw angles and wake contours of the Guishan OWF under the three typical wind speeds and directions are shown in Fig. 13. The corresponding output powers and CFs of the Guishan OWF under the three typical inflow wind conditions are given in Table 4.

Table 4

Output powers and CFs of the Guishan OWF before and after AYC

Wind condition	Before AYC		After AYC		Power increment percentage
	P_{OWF} (MW)	CF_{OWF}	P_{OWF} (MW)	CF_{OWF}	
Case 1	23.30	11.47%	29.11	14.33%	24.89%
Case 2	83.50	41.10%	85.28	41.98%	2.13%
Case 3	156.11	76.84%	159.97	78.74%	2.47%

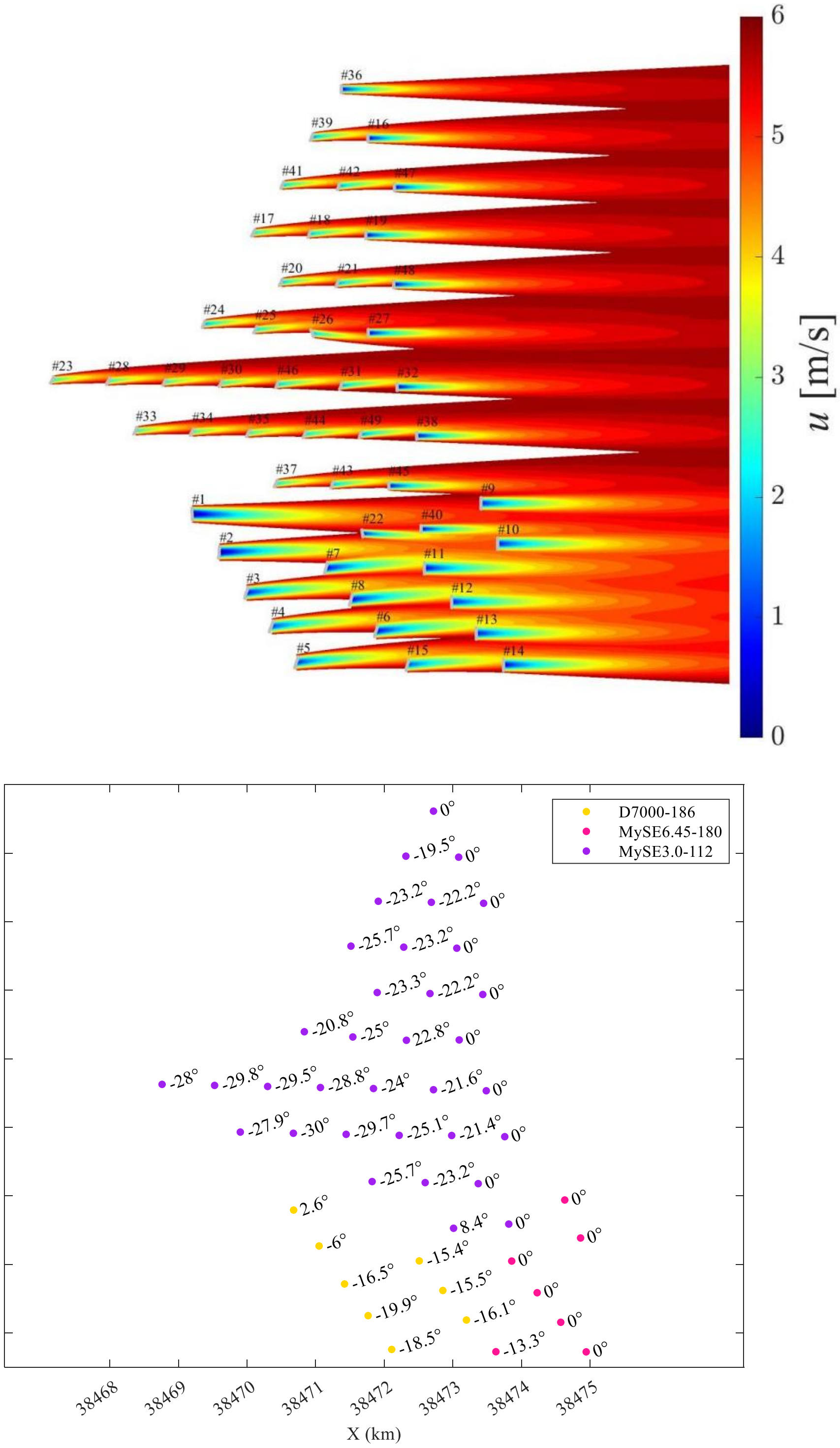

(a) Case 1: $\theta = \mathrm{W}, u_0 = 6$ m/s

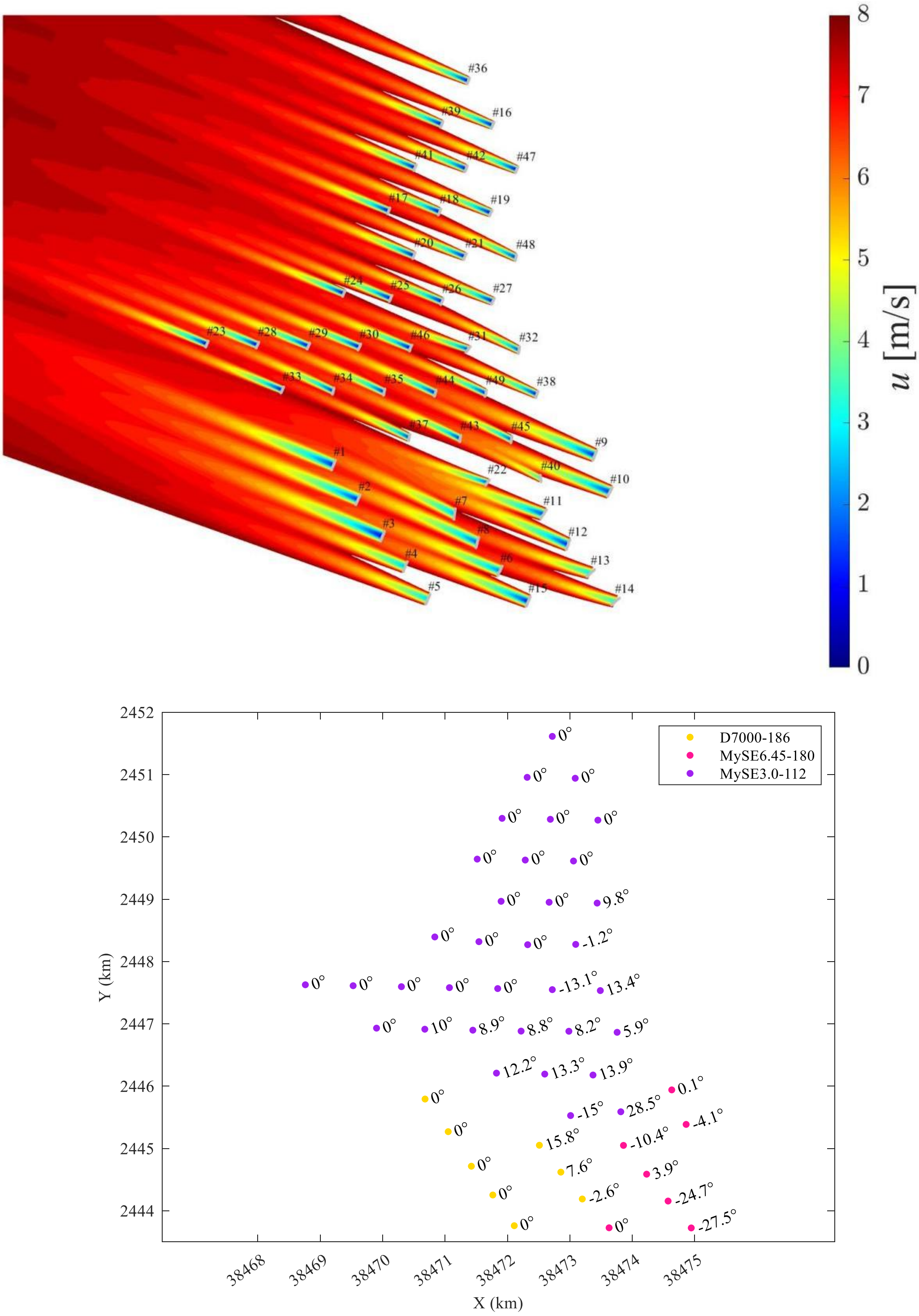

(b) Case 2: $\theta = \mathrm{ESE}, u_0 = 8$ m/s

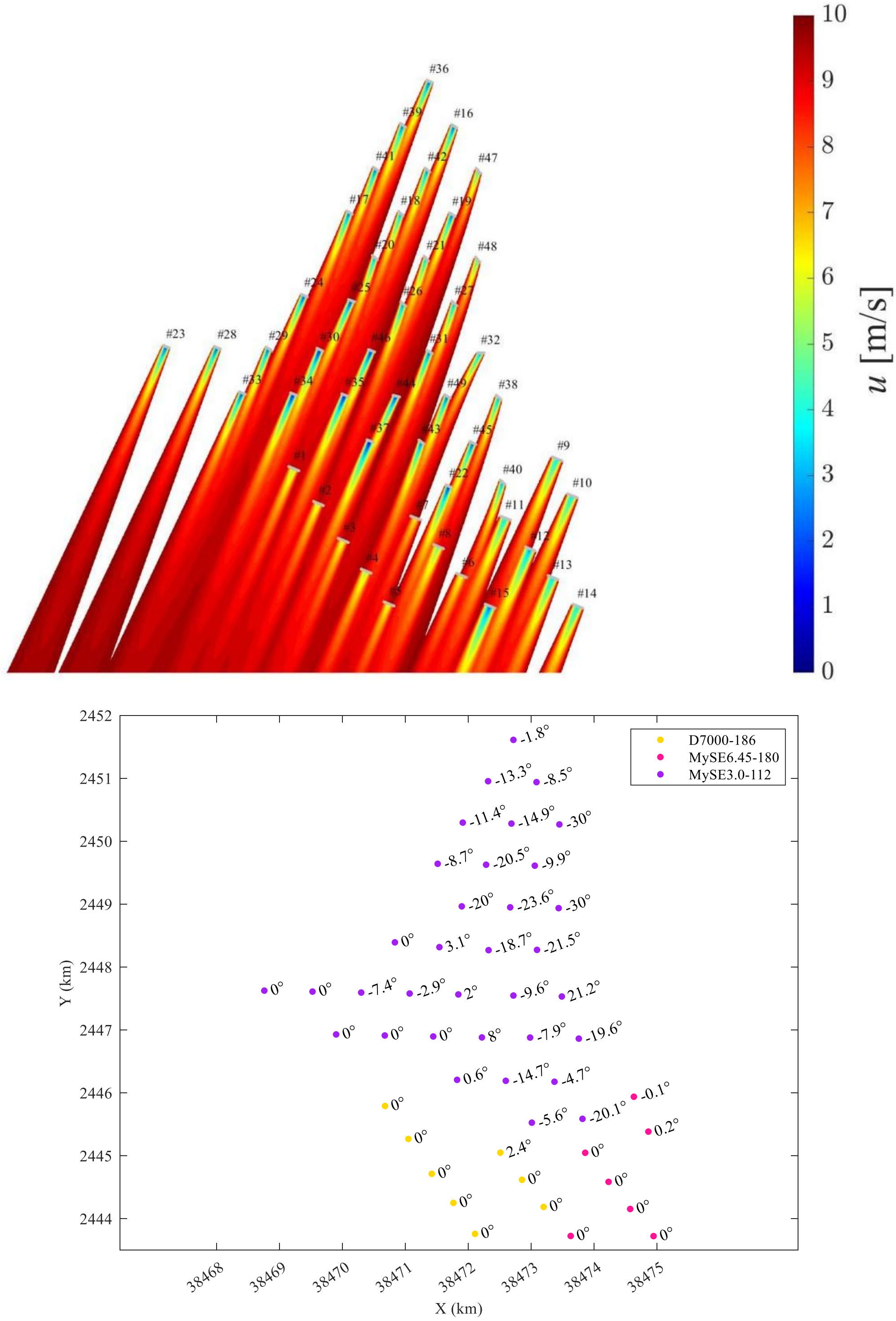

(c) Case 3: $\theta = \mathrm{NNE}, u_0 = 10\ \mathrm{m/s}$

Fig. 13. Optimal WT wake contours and yaw angles of the Guishan OWF under typical wind speeds and wind directions.

Firstly, in the dominant wind direction and under the high wind speed (Case 3: $\theta = \text{NNE}, u_0 = 10\ \text{m/s}$), the hybrid OWF can produce the maximum power after AYC which is an evident outcome. Within operational limits, higher wind speed enables WTs to capture more wind energy and generate greater electricity which follows the "$P_{wt} \propto u_0^3$" relationship until reaching the rated power. However, the power increment percentage reaches the maximum (24.89%) after AYC in the rare wind direction and under the low wind speed (Case 1: $\theta = \text{W}, u_0 = 6\ \text{m/s}$) which means AYC demonstrates more pronounced effects in the non-dominant wind directions. This can be explained by taking two aspects into account. On one hand, there exists marginal benefit differences in wake management among different wind directions. The OWF layout is aerodynamically optimized in the dominant wind directions via staggered configurations where wake effects are already mitigated, leaving marginal (1-2%) energy capture improvement potential through AYC. In contrast, for the non-dominant wind directions where the OWF layout is sub-optimal, wake steering via AYC can mitigate 10-20% of the otherwise occurring downstream power deficits. On the other hand, in the non-dominant wind directions, the power response to yaw misalignment is more gradual due to pre-reduced aerodynamic efficiency, while wake deflection exhibits heightened sensitivity, *i.e.*, each degree of yaw generates proportionally greater wake redirection.

Secondly, as shown clearly in Fig. 13 that the optimal yaw angles of the WTs in the last row remain zero under the three typical inflow wind directions. This finding is consistent with the previous test cases of three WTs aligned in a row. Three key factors contributed to this outcome. First, the WTs in the last row at the far downstream end of the OWF experience no wake interference on subsequent WTs, eliminating the need for AYC. Aligning perfectly with the incoming wind direction ($\gamma = 0°$) can maximize their own energy capture efficiency. Maintaining zero yaw angle for the last row of WTs reduces lateral wake interference in downstream WT-free areas, preventing unnecessary energy losses. Applying dynamic AYC across all WTs in the whole OWF might induce system oscillations or instability. Fixing the last-row WTs at zero yaw angle can reduce control dimensionality and enhance system robustness.

Finally, Cases 1 and 3 demonstrate that the front-row WTs, which are the first to encounter incoming wind flows exhibit significantly larger optimal yaw angles in smaller models (MySE3.0-112) compared to their utility-scale counterparts (MySE6.45-180 and D7000-186) as shown in Figs. 12 (a)(c). This is in accordance with the conclusion obtained from the previous test cases of three WTs aligned in a row which further validates that the application of AYC for small WTs is more cost-effective than that for the large WTs in a hybrid OWF.

The convergence performance of the QGA when solving the hybrid OWF AYC optimization problems in Fig. 13 is compared with the GA, the particle swarm optimization (PSO), the differential evolution (DE) [41], and the teaching learning-based optimization (TLBO) [22] algorithms. The population size $nPop$ and the maximum iteration number $MaxIt$ are set 200 and 300 respectively for all the algorithms. In the GA and DE algorithms, the crossover rate is set $p_c = 0.75$ and the mutation probability is set $p_m = \frac{1}{24}$ which is the same as those in the QGA. In the PSO algorithm, the personal learning coefficient is set $c_1 = 1.5$ and the global learning coefficient is set $c_2 = 2.0$. The best fitness evaluations in each iteration for solving the hybrid OWF AYC model after 20 times of executing these five algorithms are shown and compared in Fig. 14 and Table 5. The computations are carried out on a Windows 10 laptop with 8.0 GB RAM and a 2.40 GHz Intel Dual-Core processor and the simulation software is MATLAB 2024b.

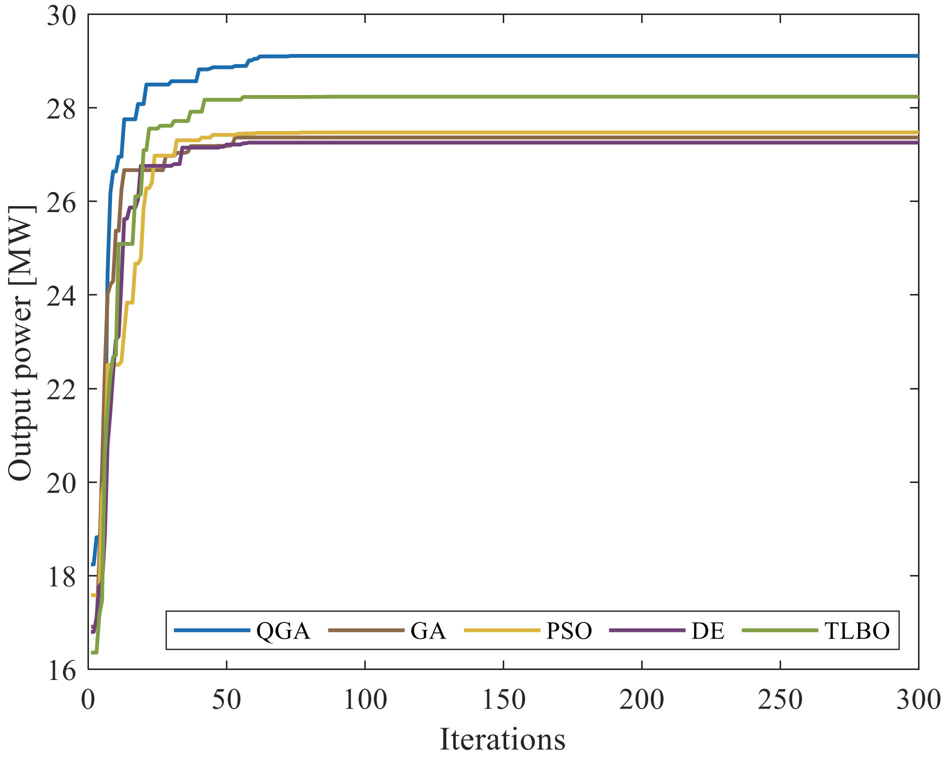

(a) Case 1: $\theta = \mathrm{W}, u_0 = 6$ m/s

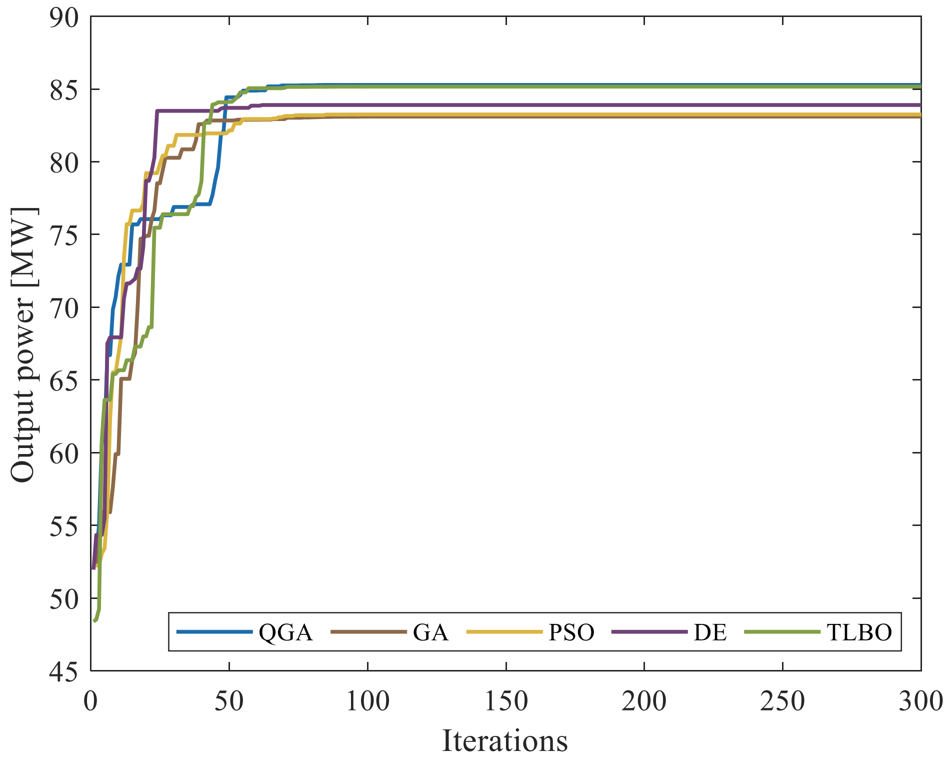

(b) Case 2: $\theta = \mathrm{ESE}, u_0 = 8\ \mathrm{m/s}$

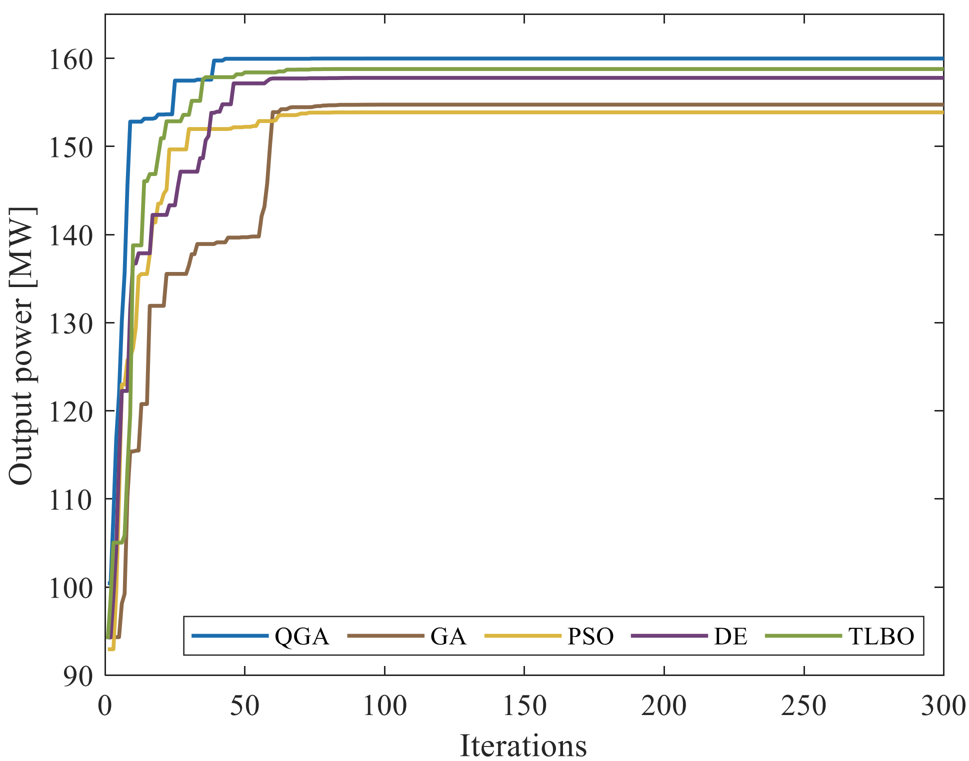

(c) Case 3: $\theta = \mathrm{NNE}, u_0 = 10\ \mathrm{m/s}$

Fig. 14. Convergence curves of the QGA, GA, PSO, DE and TLBO algorithms in solving the hybrid OWF AYC optimization problems in Fig. 13.

Table 5

Comparison of the QGA, GA, PSO, DE and TLBO algorithms in solving the hybrid OWF AYC optimization problems in Fig. 13.

Wind condition	Algorithm	Power increment percentage	Running time (min)
Case 1: $\theta =$ W, $u_0 = 6$ m/s	QGA	+24.89%	17.83
	GA	+17.45%	25.78
	PSO	+17.92%	23.11
	DE	+16.98%	20.96
	TLBO	+21.19%	19.04
Case 2: $\theta =$ ESE, $u_0 = 8$ m/s	QGA	+2.13%	20.12
	GA	-0.47%	28.31
	PSO	-0.30%	25.98
	DE	+0.48%	23.66
	TLBO	+1.99%	21.97
Case 3: $\theta =$ NNE, $u_0 =$ 10 m/s	QGA	+2.47%	19.30
	GA	-0.88%	27.76
	PSO	-1.44%	24.58
	DE	+1.07%	22.61
	TLBO	+1.71%	20.97

As shown in Fig. 14 the QGA outperforms both the other four algorithms in terms of producing the best results. By integrating quantum computing principles, the QGA enhances the efficiency and effectiveness of the optimization process. Specifically, it leverages quantum operations to address challenges inherent in classical heuristic methods. One such operation is reverse quantum annealing, which enables quasi-local or quasi-nonlocal searches initiated from a classical state. This process utilizes quantum fluctuations as a novel mutation mechanism, while classical crossover operations are retained. These quantum enhancements are the primary reasons for the QGA's superior optimization capability. For the real-time control of OWFs, a fast and efficient optimizer is critical. As wind speed and direction fluctuate, the AYC system must rapidly solve the optimization model and transmit updated control parameters to the WTs for yaw angle adjustment which is a process requiring completion within seconds. The high efficiency of the QGA is therefore essential for this application.

As shown in Table 5, the QGA achieves the highest OWF power increment percentage while requiring the shortest running time among all five algorithms. The TLBO and DE algorithms rank as the second and third best-performing methods, respectively, while the GA and PSO algorithms demonstrate comparatively poorer performance. What should be noticed is that in Cases 2 and 3, the GA and the PSO algorithms even produce results with negative power increment percentages which means they may stuck in the local optimal and fail to find the global optimum. This verifies that the QGA and TLBO are superior optimization tools for hybrid OWF AYC optimization problems, while GA and PSO prove incompetent.

From the above simulations and existing literature [22]-[42], it can be concluded that AYC generally leads to an increase in OWF power output. The three lined-up WTs and the irregular-shaped Guishan OWF tested in this paper have already validated the effectiveness of the proposed AYC strategy. For OWFs with other complex layouts, such as square [24][31][39], triangle [23][25][32], parallelogram [22][26][32][34][35][39], and other irregular shapes [24][25][30][31][33][35][36][37][41][42], AYC proves capable of boosting power generation in both large-scale and multi-scenario cases.

5. Conclusions

This paper proposes an AYC strategy specifically designed for the hybrid OWF where multiple types of WTs are installed. To achieve the goal of OWF output power maximization, a 3D yawed wake model is utilized and the QGA is applied for solving the AYC optimization models. The key findings from the simulation results of the case study and their implications for engineering applications can be summarized as follows.

1) The primary objective of AYC is to optimize the overall OWF power production. For the upstream WTs, active yaw misalignment (*e.g.*, $\gamma = \pm 30°$) can deflect wakes away from critical downstream paths, minimizing impact on subsequent WTs. For the downstream WTs, priority shifts to maximizing individual energy capture, as wake steering provides no further benefit. Especially, no active yaw misalignment should be applied to the WTs in the last row ($\gamma = 0°$).

2) AYC is more effective when inflow wind speed is at low level and in the non-dominant wind direction of an OWF. In the Guishan OWF, it produces 24.89% power increment under the wind condition of $\theta = \mathrm{W}, u_0 = 6\ \mathrm{m/s}$, much higher than those (2.13% and 2.47%) obtained under the wind conditions of $\theta = \mathrm{ESE}, u_0 = 8\ \mathrm{m/s}$ and $\theta = \mathrm{NNE}, u_0 = 10\ \mathrm{m/s}$. Although non-prevailing winds occur infrequently (*e.g.*, only 10% of annual operating

time), they may account for 25-40% of total energy losses in a hybrid OWF. Under these wind directions, wake overlap is more severe because WT sub-optimal layout and conventional yaw systems exhibit delayed response. Therefore, the application of AYC in the non-dominant wind directions of hybrid OWFs should be prioritized for the technical and economic considerations.

3) For three WTs with different types in a line, by applying the AYC strategy to the sequences with the smallest WT being the first, the maximal power increment percentages 38.15%, 28.90%, and 17.43% can be achieved for $u_0 = 6\,\mathrm{m/s}$, $8\,\mathrm{m/s}$ and $10\,\mathrm{m/s}$, respectively. For a hybrid OWF mixed-installed with multiple types of WTs, the AYC should be preferentially applied to the small WTs. By prioritizing AYC of small WTs, *e.g.*, actively deflecting them at specific angles, the wake can be dispersed or redirected, thereby mitigating its shading effect on downstream large WTs. Specifically, in a hybrid OWF, small WTs can act as 'wake regulators' dynamically adjusting their yaw to optimize the overall OWF flow field, while large WTs maintain stable operation to ensure the baseline power output of the OWF.

4) The QGA proves to be an efficient heuristic algorithm for solving the hybrid OWF AYC optimization problem. Compared with the GA, PSO, DE and TLBO algorithms, the QGA can produce the best optimization results by taking the least running time of 17.83 min, 20.12 min, and 19.30 min for the

three simulation cases, respectively, while the GA and PSO algorithms are easier to fall into local optimum. Particularly, in large-scale OWFs with multiple types and numbers of WTs, the computational burden stems primarily from the iterative calculation of wake deficits required to explore potential yaw angles. These significantly increased computational demands necessitate the development and utilization of highly efficient optimization algorithms capable of rapid convergence and the discovery of superior solutions.

However, this study still has some limitations. Firstly, the effectiveness of the proposed AYC strategy is highly related to the layout and shape of the hybrid OWF. For larger OWFs of complex layouts and installed with more WTs, the applicability of the proposed method has not been verified. Secondly, only three typical wind conditions are considered and the real-time control with smaller timescale wind data have not been tested in this study. Future research should focus on the development of more advanced AYC strategies for the hybrid OWF power increasing. The hierarchical control strategy is an ideal solution for coordinated AYC for the small and large WTs which means that the large ones employ the conventional yaw control, *e.g.*, based on average wind direction, while the small ones utilize advanced control algorithms, *e.g.*, the model predictive control (MPC) for dynamic optimization. The synergy between these approaches may enhance the overall efficiency of the hybrid OWF.

References

[1] Global Offshore Wind Report. Global Wind Energy Council, 1000 Brussels, Belgium, 2024 [Online]. Available: https://www.apren.pt/contents/publicationsothers/gwec-gowr-2024-digital-final-2-compressed-1.pdf.

[2] S. Tao, J. Yang, G. Zheng, et al. A two-stage optimization model for floating offshore wind farm layout and control. Renewable Energy 253(2025) 123614.

[3] B. Lu, X. Shen, Y. Du, et al. Offshore wind farm micro-siting based on two-phase hybrid optimization. Applied Energy 381(2025) 125105.

[4] P. Li, Y. Che, A. Hua, et al. A data-physics hybrid-driven layout optimization framework for large-scale wind farms. Applied Energy 392(2025) 125908.

[5] S. Tao, A. Feijóo-Lorenzo. Optimal layout of offshore wind farm cluster: A three-stage game model with priori coalition. IEEE Transactions on Industrial Informatics 20(7)(2024) 9225-9234.

[6] L. Shen, P. Zhou, Y. Han, et al. Wind farm layout optimization based on dynamic Levy sparrow search algorithm: A multi-parameter analysis with active yaw control. Energy 324(2025) 135989.

[7] Y. Zhang, Z. Zhang, R. Zhong, et al. Under complex wind scenarios: Considering large-scale wind turbines in wind farm layout optimization via self-adaptive optimal fractional-order guided differential evolution. Energy 323(2025) 135866.

[8] S. Tao, Q. Xu, A. Feijóo, et al. Nonuniform wind farm layout optimization: a state-of-the-art review. Energy 209(2020) 118339.

[9] M. Abdulrahman, D. Wood. Investigating the power-COE trade-off for wind farm layout optimization considering commercial turbine selection and hub height variation. Renewable Energy 102(2017) 267-278.

[10] A. Vasel-Be-Hagh, C. Archer. Wind farm hub height optimization. Applied Energy 195(2017) 905-921.

[11] M. Song, K. Chen, J. Wang. Three-dimensional wind turbine positioning using Gaussian particle swarm optimization with differential evolution. Journal of Wind Engineering and Industrial Aerodynamics 172(2018) 317-324.

[12] J. Feng, W. Shen. Design optimization of offshore wind farms with multiple types of wind turbines. Applied Energy 205(2018) 1283-1297.

[13] L. Wang, M. Cholette, Y. Fu, et al. Combined optimization of continuous wind turbine placement and variable hub height. Journal of Wind Engineering and Industrial Aerodynamics 180(2018) 136-147.

[14] S. Tao, C. Zhang, A. Feijóo-Lorenzo, et al. Wind farm repowering optimization: a techno-economic-aesthetic approach. IET Renewable Power Generation 17(8)(2023) 2137-3147.

[15] H. Sun, H. Yang, X. Gao. Investigation into spacing restriction and layout optimization of wind farm with multiple types of wind turbines. Energy 168(2019) 637-650.

[16] A. Stanley, A. Ning. Coupled wind turbine design and layout optimization with nonhomogeneous wind turbines. Wind Energy Science 4(2019) 99-114.

[17] L. Huang, H. Tang, K. Zhang, et al. 3-D layout optimization of wind turbines considering fatigue distribution. IEEE Transactions on Sustainable Energy 11(2020) 126-135.
[18] A. Ribeiro, P. Hallak, A. Lemonge, et al. Automatic grouping of wind turbine types via multi-objective formulation for nonuniform wind farm layout optimization using an analytical wake model. Energy Conversion and Management 315(2024) 118759.
[19] D. Zhang, Z. Liu, Y. Liang, et al. Bilevel optimization of non-uniform offshore wind farm layout and cable routing for the refined LCOE using an enhanced PSO. Ocean Engineering 299(2024) 117244.
[20] H. Sun, H. Yang. Wind farm layout and hub height optimization with a novel wake model. Applied Energy 348(2023) 121554.
[21] A. de Moura Ribeiro, P. Hallak, A. de Castro Lemonge, et al. Automatic grouping of wind turbine types via multi-objective formulation for nonuniform wind farm layout optimization using an analytical wake model. Energy Conversion and Management 315(2024) 118759.
[22] R. Balakrishnan, E. Son, S. Hur. Optimization of wind farm power output using wake redirection control. Renewable Energy 235(2024) 121357.
[23] K. Chen, J. Lin, Y. Qiu, et al. Model predictive control for wind farm power tracking with deep learning-based reduced order modeling. IEEE Transactions on Industrial Informatics 18(11)(2022) 7484-7493.
[24] W. Cai, Y. Hu, F. Fang, et al. Wind farm power production and fatigue load optimization based on dynamic partitioning and wake redirection of wind turbines. Applied Energy 339(2023) 121000.
[25] B. Li, J. He, M. Ge. Study of three wake control strategies for power maximization of offshore wind farms with different layouts. Energy Conversion and Management 368(2022) 116059.
[26] B. Dou, T. Qu, L. Lei, et al. Optimization of wind turbine yaw angles in a wind farm using a three-dimensional yawed wake model. Energy 209(2020) 118415.
[27] R. He, H. Yang, S. Sun, et al. A machine learning-based fatigue loads and power prediction method for wind turbines under yaw control. Applied Energy 326(2022) 120013.
[28] R. He, H. Yang, L. Lu. Optimal yaw strategy and fatigue analysis of wind turbines under the combined effects of wake and yaw control. Applied Energy 337(2023) 120878.
[29] W. Shen, J. Lin, Y. Jiang, et al. A novel yaw wake model for wind farm control applications. Renewable Energy 218(2023) 119465.
[30] H. Dong, X. Zhao. Reinforcement learning-based wind farm control: Toward large farm applications via automatic grouping and transfer learning. IEEE Transactions on Industrial Informatics 19(12)(2023) 11833-11845.
[31] H. Dong, X. Zhao. Data-driven wind farm control via multiplayer deep reinforcement learning. IEEE Transactions on Control Systems Technology 31(3)(2023) 1468-1475.
[32] Y. Wang, S. Wei, W. Yang, et al. Adaptive economic predictive control for offshore wind farm active yaw considering generation uncertainty. Applied Energy 352(2023) 121849.

[33] Q. Wang, T. Xu, D. Terzi, et al. Synchronized optimization of wind farm start-stop and yaw control based on 3D wake model. Renewable Energy 223(2024) 120044.
[34] Z. Zhang, P. Huang, G. Bitsuamlak, et al. Analytical solutions for yawed wind-turbine wakes with application to wind-farm power optimization by active yaw control. Ocean Engineering 304(2024) 117691.
[35] S. Li, A. Robert, A. Aldo Faisal, et al. Learning to optimise wind farms with graph transformers. Applied Energy 359(2024) 122758.
[36] N. Kayedpour, J. Kooning, A. Samani, et al. An optimal wind farm operation strategy for the provision of frequency containment reserve incorporating active wake control. IEEE Transactions on Sustainable Energy 15(1)(2024) 276-289.
[37] A. Hosseini, D. Cannon, A. Vasel-Be-Hagh. Wind farm active wake control via concurrent yaw and tip-speed ratio optimization. Applied Energy 377(2025) 124625.
[38] Y. Tu, Y. Chen, K. Zhang, et al. A multi-fidelity framework for power prediction of wind farm under yaw misalignment. Applied Energy 377(2025) 124600.
[39] Z. Huang, W. Wu. Dual-stage MPC-based AGC for wind farm considering aerodynamic interactions. IEEE Transactions on Sustainable Energy 16(2)(2025) 1098-1113.
[40] T. Göçmen, J. Liew, E. Kadoche, et al. Data-driven wind farm flow control and challenges towards field implementation: A review. Renewable and Sustainable Energy Reviews 216(2025) 115605.
[41] Y. Wang, Z. Liu. Fatigue analysis of wind turbine and load reduction through wind-farm-level yaw control. Energy 326(2025) 136266.
[42] S. He, H. Wang, J. Yan, et al. A low-computational physics-guided deep learning model for wind farm flow control under time-varying wind conditions. Energy 332(2025) 137048.
[43] R. Ibarrondo, G. Gatti, M. Sanz. Quantum genetic algorithm with individuals in multiple registers. IEEE Transactions on Evolutionary Computation 28(3)(2024) 788-797.
[44] Global Offshore Map. 4C Offshore. [Online]. Available: https://map.4coffshore.com/offshorewind/.
[45] Wind Turbine Models. [Online]. Available: https://wind-turbine-models.com.
[46] Xihe Energy Meteorological Big Data Platform. [Online]. Available: https://xihe-energy.com/.